On the buckling and post-buckling of core-shell cylinders under thermal loading

Fan Xu, Radhi Abdelmoula, Michel Potier-Ferry

On the buckling and post-buckling of core-shell cylinders under thermal loading

Fan Xu [a], Radhi Abdelmoula [b], Michel Potier-Ferry [c]

[a] *Institute of Mechanics and Computational Engineering, Department of Aeronautics and Astronautics, Fudan University, 220 Handan Road, Shanghai 200433, PR China*
[b] *Laboratoire des Sciences des Procédés et des Matériaux, LSPM, UPR CNRS 3407, Université Paris-Nord, 99 Avenue J.B. Clément, Villetaneuse 93430, France*
[c] *Laboratoire d'Etude des Microstructures et de Mécanique des Matériaux, LEM3, UMR CNRS 7239, Université de Lorraine, 7 Rue Félix Savart, BP 15082, 57073 Metz Cedex 03, France*

There has been a strong and recent research activity to obtain tunable wrinkling patterns in film/substrate systems, which proposes to use geometric curvature as a control parameter. This paper studies core-shell cylindrical systems under thermal loads, with the aim to describe possible wrinkling modes, bifurcation diagrams and dimensionless parameters influencing the response of the system. In the companion case of axially compressed core-shell cylinders, it was established that instability modes can be axisymmetric or diamond-like, the post-buckling response of the system is governed by a single dimensionless parameter C_s, and the bifurcation becomes supercritical for a sufficiently stiff core. In the present case of cylindrical core-shells subjected to thermal loading, one finds quite different buckling patterns, named churro-like modes that are characterized by a fast undulation in the circumferential direction. There exists another curvature-related influencing parameter C_t, and a subcritical to supercritical bifurcation transition is observed when the core stiffness increases. The problem is analyzed both theoretically and numerically based on finite element calculations. Lastly, the obtained instability modes remain about the same as in pure shell structures, the main difference being the stabilization of the post-bifurcation behavior.

Keywords:
Post-buckling
Core-shell cylinder
Bifurcation analysis
Continuation technique
Thermal wrinkling

1. Introduction

Quantitative characterization of wrinkling process for film/substrate systems has motivated considerable research interests during past few years for understanding and predicting pattern formation both in nature (Mahadevan and Rica, 2005; Efimenko et al., 2005; Yin et al., 2009; Wang and Zhao, 2015; Zhang et al., 2016; Sáez and Zöllner, 2017) and in modern industry (Brau et al., 2011; Cai et al., 2011; Cao and Hutchinson, 2012; Sun et al., 2012; Zang et al., 2012; Xu et al., 2014; 2015a; 2015b; Fu and Cai, 2015; Xu and Potier-Ferry, 2016a; Huang et al., 2016). Broad applications range from micro/nano-fabrication of flexible electronic devices with functional surface patterning (Bowden et al., 1998; Rogers et al., 2010; Li, 2016), microlens arrays production (Chan and Crosby, 2006), adaptive aerodynamic drag control (Terwagne et al., 2014), to the mechanical property measurement of material characteristics (Howarter and Stafford, 2010). Most previous theoretical and computational works are concerned with planar film/substrate systems and suggest that wrinkling patterns strongly depend on applied loading (Chen and Hutchinson, 2004; Huang et al., 2005; Audoly and Boudaoud, 2008; Brau et al., 2011; Cai et al., 2011; Cao and Hutchinson, 2012; Xu et al., 2014; 2015b). Recent investigations revealed that wrinkling patterns may also vary with the substrate curvature (Yin et al., 2009; Chen and Yin, 2010; Li et al., 2011; Breid and Crosby, 2013; Terwagne et al., 2014; Jia et al., 2015) so that much attention has been paid to explore curvature effects on mode selection in non-planar film/substrate systems (Zhao et al., 2014; Patrício et al., 2014; Stoop et al., 2015; Xu and Potier-Ferry, 2016b; Shao et al., 2016), which demonstrates the important impacts of the topological constraints of curved geometry on instability patterns. For instance, a planar film/substrate bilayer usually exhibits sinusoidal wrinkling patterns under uniaxial compression. Nevertheless, considering a core-shell soft cylinder subjected to axial compression, surface wrinkles may form in both axial and circumferential directions due to curvature effect, leading to the evolution from axisymmetric sinusoidal wrinkles to non-axisymmetric diamond-like mode, which depends on one single dimensionless parameter $C_s = (E_s/E_f)(R/h_f)^{3/2}$ that

is a function of modulus ratio and curvature of the structure (Xu and Potier-Ferry, 2016b). This suggests that geometric curvature and modulus effects play a key role in pattern formation in curved surfaces, especially the core-shell cylinder that appears to be the simplest structure with zero Gaussian curvature, which deserves further investigations.

In history, the nonlinear buckling and post-buckling analysis of thin-walled circular cylindrical shells under various loading conditions has received considerable attention (von Kármán and Tsien, 1941; Koiter, 1945; Hutchinson and Koiter, 1970; Yamaki, 1984; Bushnell, 1985), with the most representative loadings being the axial compression and external pressure. Circular shell cylinders subjected to axial compression can be characterized by a high buckling stress ($\sigma_{cr} \approx 0.605Eh/R$), short-wavelength instability patterns ($\ell_w \approx \sqrt{Rh}$) and a very strong imperfection-sensitivity associated with an extremely unstable post-buckling behavior. The importance of this nonlinear post-bifurcation property has been early recognized since 1940s (von Kármán and Tsien, 1941; Koiter, 1945). In the simplest bifurcation analysis, many buckling modes coincide, including axisymmetric and diamond-like shapes. The co-existence of these two pattern types is typical of cylindrical geometry and it has been observed both in pure shell and core-shell structures. However, the presence of a stiff core ($C_s \geq 0.9$) leads to sinusoidally deformed axisymmetric patterns that rarely appear in pure shells without a core. In the literature on shell buckling, curvature effect is often accounted through the dimensionless Batdorf parameter $Z = L^2\sqrt{1-\nu^2}/(Rh)$ (Batdorf, 1947; Yamaki, 1984; Bushnell, 1985; Abdelmoula et al., 1992; Abdelmoula and Leger, 2008). There are a large number of references on the buckling of circular cylindrical shells, namely a few textbooks (Yamaki, 1984; Bushnell, 1985; Julien, 1991; Teng and Rotter, 2006; Koiter, 2009), review papers (Hutchinson and Koiter, 1970; Arbocz, 1987; Teng, 1996) and a website named 'Shell Buckling' (Bushnell and Bushnell, 2015).

When a cylindrical shell is filled with a soft core, *i.e.* a core-shell soft cylinder, short-wavelength bifurcation modes can be persistently observed experimentally and numerically in both buckling and post-buckling stages, and the unstable post-bifurcation behavior can be stabilized by the presence of a core (Zhao et al., 2014; Xu and Potier-Ferry, 2016b). There exist a few contributions on the buckling analyses of a cylindrical shell filled with a soft core, which either study the stabilizing effects of soft cores on the buckling strength of shells (Yao, 1962; Myint-U, 1969) or focus on axisymmetric instability modes (Karam and Gibson, 1995; Ye et al., 2011; Wu et al., 2012). Core-shell cylinders subjected to axial compression have been thoroughly studied theoretically and numerically from a quantitative point of view in the recent work (Xu and Potier-Ferry, 2016b), where the critical parameter C_s determines a phase diagram of axisymmetric/diamond-like mode transition. For a stiff core ($C_s \geq 0.9$), the buckling pattern is axisymmetric and post-bifurcation solutions are stable; whereas for a soft core ($C_s \leq 0.7$), the bifurcated solution branch is often subcritical and the associated instability modes tend to be diamond shaped after secondary bifurcations. The stabilization of post-bifurcation patterns turns out to be the major consequence of the presence of a core.

Deviating from the axial compression case, circular cylindrical shells under external pressure or thermal loading would show a totally different mechanical response with oscillations varying much faster in circumferential direction than in the axial direction. In other words, the wavelength in the axial direction can be global ($\ell_x \approx L$), while it is quite local in the circumferential direction ($\ell_y \ll \ell_x$), in the order of $\ell_y \sim L^{1/2}(Rh)^{1/4}$ (Abdelmoula and Leger, 2008). This implies that the explicit expression of this critical parameter C_s may change its form and has to be re-defined. Besides, this parameter would significantly affect supercritical/subcritical post-bifurcation response of core-shell cylindrical structures and requires to be thoroughly studied. As the instability mode is not local, the influence of boundary conditions becomes more important than that in the case of axial compression, which induces boundary layers (Abdelmoula and Leger, 2008) and some strange effects of boundary conditions (Sobel, 1964). These features will be discussed in the present case of core-shell cylinders.

This paper aims at exploring the occurrence and post-buckling evolution of 3D wrinkling patterns in core-shell soft cylindrical structures subjected to thermal loading, through applying advanced numerical methods from a quantitative standpoint. Theoretical analyses based on the well-known nonlinear Donnell–Mushtari–Vlassov (DMV) shell formulations are first carried out to qualitatively determine dimensionless parameters that influence the instability patterns. Spatial pattern formation is then quantitatively investigated based on a nonlinear 3D finite element model, associating geometrically nonlinear shell formulations for the surface layer and linear elastic solids for the core, and a robust path-following continuation technique called Asymptotic Numerical Method (ANM) (Damil and Potier-Ferry, 1990; Cochelin et al., 1994; Cochelin, 1994; Cochelin et al., 2007). The same finite element procedure has been validated and applied previously in Xu et al. (2014); Xu and Potier-Ferry (2016b). Here we consider geometrically perfect core-shell structures without any imperfection. The paper is organized as follows. In Section 2, a nonlinear finite element model is concisely presented. Section 3 is devoted to several theoretical analyses within the framework of the DMV shell formulations and the Biot - Winkler assumption on the substrate. First, one recalls why the buckling mode depends strongly on the loading type and one explains why it has consequence on dimensional analyses. A simplified core-shell model, established in the same way as in Abdelmoula et al. (1992), allows deducing the buckling stress and the post-buckling behavior of the system. Numerical calculations are presented in Section 4, including the deformation shape of buckling patterns, bifurcation scenario and the influence of leading parameters.

2. Numerical model

The 3D core-shell cylindrical system will be analyzed by a nonlinear finite element model, which was first introduced in Xu et al. (2014) and then applied to hyperelastic film/substrate (Xu et al., 2015a) as well as core-shell cylindrical system (Xu and Potier-Ferry, 2016b). This finite element framework appears to be sufficiently versatile for the present case of circular cylindrical geometry and thermal loading. In this model, the surface layer is represented by a thin shell model to allow large rotations, while the core is modeled by small strain elasticity. Indeed, the considered instabilities are governed by nonlinear geometric effects for the stiff material, while the effects are much smaller for the soft material. For planar film/substrate systems, a thorough investigation on comparison between finite strain hyperelastic model and small strain elastic model, with respect to a wide range of Young's modulus, was carried out in Xu et al. (2015a). It demonstrates that deformation of the system can be relatively large and finite strain constitutive laws have to be taken into account, if the stiffness ratio is rather small, *e.g.* $E_f/E_s \approx \mathcal{O}(10)$. In most cases of film/substrate systems, *i.e.* $E_f/E_s \gg \mathcal{O}(10)$, small strain elastic models appear to be sufficient and are qualitatively or even quantitatively equivalent to finite strain hyperelastic models. This remains valid for core-shell soft cylindrical structures as well, as seen in Zhao et al. (2014); Xu and Potier-Ferry (2016b). Therefore, in what follows, we consider Hookean elasticity for the potential energy of the system for simplicity.

Challenges in the numerical modeling of such core-shell cylindrical systems come from large aspect ratio ($2\pi R/h_f \geqslant \mathcal{O}(10^2)$,

$L/h_f \geqslant \mathcal{O}(10^2)$) and radius/thickness ratio ($R/h_f \geqslant \mathcal{O}(10)$), which require very fine meshes if employing 3D brick elements for both the surface and the core. Since finite rotations of middle surface and small strains are considered in the surface layer, nonlinear shell formulations are quite suitable and efficient for modeling. In this part, a shell formulation in curvilinear coordinates, which is proven to be suitable for core-shell cylinders (Xu and Potier-Ferry, 2016b) and film/substrate bilayers (Xu et al., 2014; 2015a), is applied. It is incorporated via the Enhanced Assumed Strain (EAS) concept to improve the element performance and to avoid locking phenomena such as Poisson thickness locking, shear locking or volume locking. This hybrid shell formulation can describe large rotations and large displacements, and has been successively applied to nonlinear elastic thin-walled structures such as cantilever beam, square plate, cylindrical roof and circular deep arch (Zahrouni et al., 1999; Boutyour et al., 2004).

Formulations of geometry and kinematics of the shell element can be found in Xu et al. (2014); 2015a); Xu and Potier-Ferry (2016b). The hybrid shell formulation is derived from a three-field variational principle based on the Hu–Washizu functional (Büchter et al., 1994; Zahrouni et al., 1999). The stationary condition can be written as

$$\mathbf{\Pi}_f\left(\mathbf{u}_f, \widetilde{\gamma}, \mathbf{S}\right) = \int_{\Omega_f} \left\{ {}^t\mathbf{S} : (\gamma_u + \widetilde{\gamma}) - \frac{1}{2} {}^t\mathbf{S} : \mathbf{D}^{-1} : \mathbf{S} \right\} \mathrm{d}\Omega, \tag{1}$$

where $\mathbf{D}$ is the elastic stiffness tensor of the shell. The unknowns are, respectively, the displacement field $\mathbf{u}_f$, the second Piola–Kirchhoff stress tensor $\mathbf{S}$ and the compatible Green–Lagrange strain γ_u. The enhanced assumed strain $\widetilde{\gamma}$, satisfies the condition of orthogonality with respect to the stress field.

A 8-node quadrilateral element with reduced integration is used for the 7-parameter shell formulation. The enhanced assumed strain $\widetilde{\gamma}$ neither requires inter element continuity, nor contributes to the total number of nodal degrees of freedom. Therefore, it can be eliminated by condensation at the element level, which preserves the formal structure of a 6-parameter shell theory with totally 48 degrees of freedom per element.

Since the displacement, rotation and strain remain relatively small in the core, the linear isotropic elasticity theory can accurately describe the core (Xu and Potier-Ferry, 2016b). Hence, the potential energy of the core can be expressed as

$$\mathbf{\Pi}_s(\mathbf{u}_s) = \int_{\Omega_s} \frac{1}{2} \left({}^t\varepsilon : \mathbf{L}_s : \varepsilon - {}^t\varepsilon : \mathbf{L}_s : \varepsilon_{th} \right) \mathrm{d}\Omega, \tag{2}$$

where $\mathbf{L}_s$ is the elastic matrix of the core. The total strain and thermal strain are respectively denoted as ε and ε_{th}. In this paper, 8-node linear brick elements with reduced integration are applied to discretize the core, with totally 24 degrees of freedom on each brick element. Note that the core is subjected to the thermal loading that can be expressed as

$$\varepsilon_{th} = \alpha \Delta T \mathbf{I} \quad \text{with} \quad \Delta T < 0, \tag{3}$$

where α, ΔT and $\mathbf{I}$ denote the thermal expansion coefficient, temperature change and second-order identity tensor, respectively. This thermal shrinking loading ε_{th} can be characterized by a residual strain $\varepsilon_{th} = \varepsilon_{res} = -\lambda \mathbf{I}$, while λ is a scalar load parameter and only normal strains are considered for isotropic loading.

As the surface shell is bonded to the core, the displacement should be continuous at the interface (Xu et al., 2014; Xu and Potier-Ferry, 2016b). However, the shell elements and 3D brick elements cannot be simply joined directly since they belong to dissimilar elements. Therefore, additional incorporating constraint equations have to be employed. Here, Lagrange multipliers are applied to couple the corresponding nodal displacements in compatible meshes between the shell and the core (see Fig. 1). Note that using 8-node linear brick element here is only for coupling convenience, and 20-node quadratic brick element would be another good candidate, while both of them follow the same coupling strategy. Consequently, the stationary function of the core-shell system is given in a Lagrangian form:

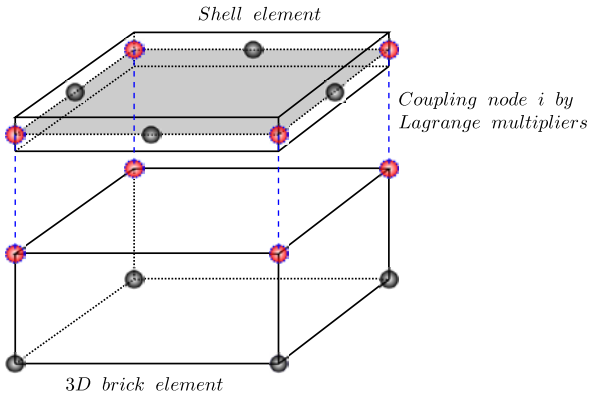

Fig. 1. Sketch of coupling at the interface. The coupling nodes are marked by red color. (For interpretation of the references to colour in this figure legend, the reader is referred to the web version of this article.)

$$\mathscr{L}(\mathbf{u}_f, \mathbf{u}_s, \ell) = \mathbf{\Pi}_f + \mathbf{\Pi}_s + \sum_{\text{node } i} \ell_i \left[\mathbf{u}_f(i) - \mathbf{u}_s(i) \right], \tag{4}$$

where the displacements of the shell and the core are, respectively, denoted as $\mathbf{u}_f$ and $\mathbf{u}_s$, while the Lagrange multipliers are represented by ℓ. From Eq. (4), three equations are obtained according to $\delta\mathbf{u}_f$, $\delta\mathbf{u}_s$ and $\delta\ell$:

$$\begin{cases} \delta\mathbf{\Pi}_f + \sum\limits_{\text{node } i} \ell_i \delta\mathbf{u}_f(i) = 0, \\ \delta\mathbf{\Pi}_s - \sum\limits_{\text{node } i} \ell_i \delta\mathbf{u}_s(i) = 0, \\ \sum\limits_{\text{node } i} \delta\ell_i \mathbf{u}_f(i) - \sum\limits_{\text{node } i} \delta\ell_i \mathbf{u}_s(i) = 0. \end{cases} \tag{5}$$

A path-following continuation technique named ANM (Damil and Potier-Ferry, 1990; Cochelin et al., 1994; Cochelin, 1994; Cochelin et al., 2007) is applied to solve the resulting nonlinear PDEs (5). The ANM is a numerical perturbation technique based on a succession of high-order power series expansions with respect to a well chosen path parameter, which appears as an efficient continuation predictor without any corrector iteration. Besides, one can get approximations of the solution path that are very accurate inside the radius of convergence. In this paper, the main interest of the ANM is its ability to trace the post-buckling evolution on the equilibrium path and to predict secondary bifurcations without any special tool. Precisely, accumulation of small steps in the ANM is often associated with the occurrence of a bifurcation (Xu et al., 2014; 2015a; 2015b; Xu and Potier-Ferry, 2016b).

3. Theoretical analyses

In this section, the buckling of a core-shell cylinder under thermal loading is analyzed theoretically. The objective is to explain the deformation shape of the corresponding buckling patterns and to highlight the dimensionless quantities which influence the buckling and post-buckling response of the core-shell system. Previous works by Zhao et al. (2014); Xu and Potier-Ferry (2016b) have demonstrated that two types of modes can be observed when the cylindrical core-shell is subjected to an axial compression: axisymmetric sinusoidal or non-axisymmetric diamond-like shape according to the value of one single dimensionless parameter $C_s = (E_s/E_f)(R/h_f)^{3/2}$. In fact, different wrinkling shapes have been obtained from the numerical framework presented in Section 2, with only one half-wave in the axial direction but short wave-length instability circumferentially (see Fig. 2). In other words, the buckling

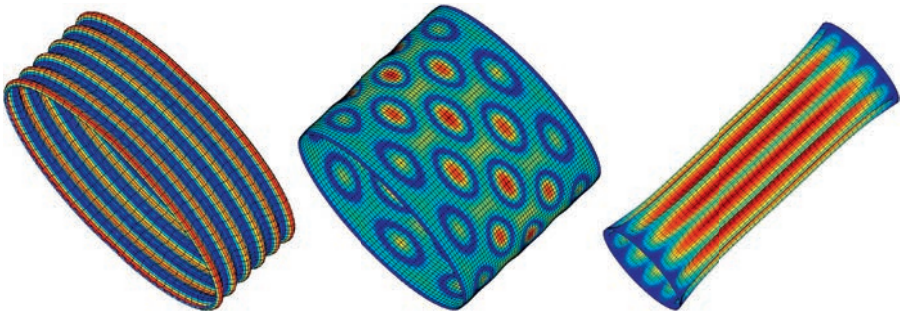

Fig. 2. Three representative instability patterns obtained from numerical calculations: (a) axisymmetric sinusoidal mode under axial compression; (b) non-axisymmetric diamond-like mode under axial compression; (c) churro-like mode under thermal loading.

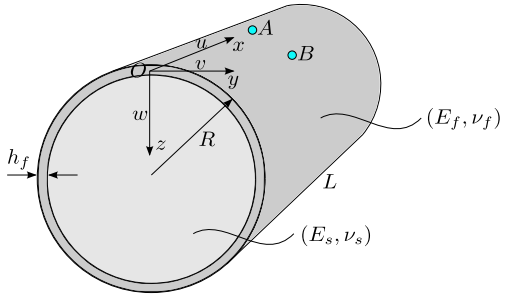

Fig. 3. Geometry of core-shell cylindrical structure.

of a core-shell cylinder under thermal loads approximates to the buckling of a cylindrical shell under external hydrostatic pressure that has been widely discussed in the literature (Batdorf, 1947; Sobel, 1964; Abdelmoula and Leger, 2008; Timoshenko and Gere, 1961; Brush and Almroth, 1975; Yamaki, 1984; Bažant and Cedolin, 1991). The explanation is simple: the thermal loading induces an isotropic stress state in the pre-buckling stage ($\sigma_x = \sigma_y$), but it is well known that the critical buckling stress is generally much higher in the axial compression case than in the external pressure situation, with the following orders of magnitude:

$$\begin{cases} \dfrac{|\sigma_x^c|}{E_f} = \dfrac{1}{\sqrt{3(1-\nu_f^2)}}\dfrac{h_f}{R} \approx 0.605\dfrac{h_f}{R} \quad \text{when} \quad \nu_f = 0.3, \\ \dfrac{|\sigma_y^c|}{E_f} = \mathcal{O}\left[\left(\dfrac{h_f}{R}\right)^{3/2}\dfrac{R}{L}\right]. \end{cases} \tag{6}$$

Thus, the circumferential stress σ_y would destabilize the system much earlier than the axial stress σ_x so that the corresponding instability pattern should be similar to the external pressure loading case. In the same way, it is known that the critical load in the lateral pressure case ($\sigma_x = 0$) is almost the same as in the hydrostatic pressure case ($\sigma_x = \sigma_y/2$) (Batdorf, 1947), which confirms the weak influence of the axial stress when the circumferential stress is compressive.

3.1. Core-shell DMV model with a foundation

We consider an elastic cylindrical shell supported by a soft core, which can buckle under external pressure p. Upon wrinkling, the shell elastically buckles to relax the compressive stress and the core concurrently deforms to maintain perfect bonding at the interface. The core-shell cylindrical system is considered to be three-dimensional and the geometry is as shown in Fig. 3. In this study, we consider the case where the thickness of the shell is much smaller than the radius of the cylinder, with $R/h_f \geqslant \mathcal{O}(10)$ as usually accounted for thin shell models. Let x and y be axial and circumferential coordinates, while z represents the radial direction coordinate. The thickness of the shell, the radius and the length of the system are denoted by h_f, R and L, respectively. Young's modulus and Poisson's ratio of the shell are respectively denoted by E_f and ν_f, while E_s and ν_s are the corresponding material properties for the core. The same frame will be adapted to the components of the displacements u, v, w, and the stress function F for stress resultants.

The Donnell - Mushtari - Vlassov (DMV) shell model (Brush and Almroth, 1975; Yamaki, 1984) that relies on the assumption of moderately large rotations and various simplifications on curvature is taken into account. It is not as general as the shell model used in the numerical calculations, but it is sufficiently accurate for buckling modes with at least four or five circumferential waves. It will be also sufficient for the qualitative analysis aimed in this section. In the version describing the membrane stress by a stress function, the governing equations read

$$\begin{cases} D\Delta^2 w - \dfrac{1}{R}\dfrac{\partial^2 F}{\partial x^2} - [F, w] = p, \\ \dfrac{1}{E_f h_f}\Delta^2 F + \dfrac{1}{R}\dfrac{\partial^2 w}{\partial x^2} + \dfrac{1}{2}[w, w] = 0, \end{cases} \tag{7}$$

where Δ^2 and $D = E_f h_f^3/[12(1-\nu_f^2)]$ respectively denote the biharmonic operator and flexural rigidities of the shell. The nonlinear Monge - Ampère operator is defined as

$$[a, b] = \frac{\partial^2 a}{\partial x^2}\frac{\partial^2 b}{\partial y^2} + \frac{\partial^2 a}{\partial y^2}\frac{\partial^2 b}{\partial x^2} - 2\frac{\partial^2 a}{\partial x \partial y}\frac{\partial^2 b}{\partial x \partial y}. \tag{8}$$

The stress function F is related to the resultant stress by

$$N_x = \frac{\partial^2 F}{\partial y^2}, \quad N_y = \frac{\partial^2 F}{\partial x^2}, \quad N_{xy} = -\frac{\partial^2 F}{\partial x \partial y}. \tag{9}$$

In a cylindrical core-shell system, the normal pressure $p(x, y)$ is a function of the normal stress on the core boundary. Nevertheless, one can avoid the elastic solid description of the core by considering a Winkler-type approach: one assumes that this normal pressure is proportional to the deflection $w(x, y)$ at the same place. By considering a sinusoidal load, Biot (Biot, 1937; Allen, 1969) established a closed form of the Winkler stiffness ratio that depends on the half buckling wavelength ℓ_w that is *a priori* unknown:

$$K_s = \frac{E_s}{(3-\nu_s)(1+\nu_s)}\frac{2\pi}{\ell_w}. \tag{10}$$

The theoretical analyses will be conducted within this framework and the core-shell system is assumed to be governed by the fol-

lowing partial differential equations (PDEs):

$$\begin{cases} D\Delta^2 w - \dfrac{1}{R}\dfrac{\partial^2 F}{\partial x^2} - [F,w] + K_s w = 0, \\ \dfrac{1}{E_f h_f}\Delta^2 F + \dfrac{1}{R}\dfrac{\partial^2 w}{\partial x^2} + \dfrac{1}{2}[w,w] = 0. \end{cases} \tag{11}$$

Various boundary conditions are concerned in the literature (Sobel, 1964) and the most used boundary conditions can be expressed as follows:

$$\begin{array}{ll} \mathbf{C}1: w = w_{,x} = u = v = 0, & \mathbf{S}1: w = w_{,xx} = u = v = 0, \\ \mathbf{C}2: w = w_{,x} = u = N_{xy} = 0, & \mathbf{S}2: w = w_{,xx} = u = N_{xy} = 0, \\ \mathbf{C}3: w = w_{,x} = v = N_x = 0, & \mathbf{S}3: w = w_{,xx} = v = N_x = 0, \\ \mathbf{C}4: w = w_{,x} = N_x = N_{xy} = 0, & \mathbf{S}4: w = w_{,xx} = N_x = N_{xy} = 0, \end{array} \tag{12}$$

in which **C** stands for clamped boundary conditions while **S** denotes simply supported ones.

3.2. Why instability patterns under thermal loading differ from axial loading?

For the sake of completeness, we briefly re-discuss the linear buckling analysis of a pure shell ($K_s = 0$) under axial compression and lateral pressure, for recalling the connection among load type, mode shape and orders of magnitude. Essentially, these results can be found in Batdorf (1947) and in several textbooks on shell buckling. One seeks bifurcations from uniformly biaxial loading states

$$\sigma_x^0 \neq 0, \sigma_y^0 \neq 0, \sigma_{xy}^0 = 0 \Longrightarrow F^0(x,y) = \frac{1}{2}\left(\sigma_y^0 x^2 + \sigma_x^0 y^2\right). \tag{13}$$

The critical states are deduced from the linearized version of (11) from $F^0(x, y)$ in Eq. (13) and $w^0(x, y) = 0$:

$$\begin{cases} D\Delta^2 w - \dfrac{1}{R}\dfrac{\partial^2 F}{\partial x^2} - h_f\left(\sigma_x^0 \dfrac{\partial^2 w}{\partial x^2} + \sigma_y^0 \dfrac{\partial^2 w}{\partial y^2}\right) = 0, \\ \dfrac{1}{E_f h_f}\Delta^2 F + \dfrac{1}{R}\dfrac{\partial^2 w}{\partial x^2} = 0. \end{cases} \tag{14}$$

The two equations in (14) can be classically combined to get one single eighth-order partial differential equation (Batdorf, 1947):

$$D\Delta^4 w + \frac{E_f h_f}{R^2}\frac{\partial^4 w}{\partial x^4} - h_f\left(\sigma_x^0 \frac{\partial^2 \Delta^2 w}{\partial x^2} + \sigma_y^0 \frac{\partial^2 \Delta^2 w}{\partial y^2}\right) = 0. \tag{15}$$

Classical double-sinusoidal modes are assumed as $w(x, y) = \sin(q_x x + \varphi_x)\sin(q_y y + \varphi_y)$. One seeks the critical stresses (assumed negative) as the smallest stresses such that Eq. (15) has a solution, which leads to the minimization with respect to the wave numbers (q_x, q_y). Thus, one can get the relation between load and wave numbers from Eq. (15):

$$h_f\left(|\sigma_x^c| q_x^2 + |\sigma_y^c| q_y^2\right) = D\left(q_x^2 + q_y^2\right)^2 + \frac{E_f h_f}{R^2}\frac{q_x^4}{\left(q_x^2 + q_y^2\right)^2}. \tag{16}$$

In the case of axial compression ($\sigma_y^0 = 0$), the bifurcation condition (16) can be expressed as

$$h_f|\sigma_x^c| = DA + \frac{E_f h_f}{R^2}\frac{1}{A}, \quad A = \left(q_x + \frac{q_y^2}{q_x}\right)^2. \tag{17}$$

The minimization of σ_x^c with respect to wave numbers is straightforward. There are lots of minima lying on the famous "Koiter circle" (Koiter, 1945) with the equation:

$$A = \left(q_x + \frac{q_y^2}{q_x}\right)^2 = \sqrt{\frac{E_f h_f}{DR^2}} = \frac{\sqrt{12(1-\nu_f^2)}}{Rh_f}. \tag{18}$$

This means that the linear stability theory can predict axisymmetric ($q_y = 0$) as well as diamond-like modes ($q_x \neq 0$, $q_y \neq 0$). A recent paper (Xu and Potier-Ferry, 2016b) has established numerically that these two types of patterns can be observed for core-shell cylinders under axial compression. Note that the wavelengths of all these modes on the Koiter circle are very short as compared with the radius of the cylinder:

$$\ell_x = \frac{2\pi}{q_x} = \mathcal{O}\left(\sqrt{Rh_f}\right), \quad \ell_y = \frac{2\pi}{q_y} = \mathcal{O}\left(\sqrt{Rh_f}\right). \tag{19}$$

The critical axial stress is the minimal value of (17), which leads to the famous formula (6).

In the case of lateral pressure ($\sigma_x^0 = 0$), the bifurcation condition (16) reads

$$h_f|\sigma_y^c| = \frac{D(q_x^2 + q_y^2)^2}{q_y^2} + \frac{E_f h_f}{R^2 q_y^2}\frac{1}{\left(1 + q_y^2/q_x^2\right)^2}. \tag{20}$$

Since the critical stress predicted by (20) is an increasing function of the axial wave number q_x, the mathematical minimum with respect to the axial wave number requires $q_x = 0$, which is not permitted by boundary conditions. In fact, the axial wavelength is of the same order as the shell length ($\ell_x = \mathcal{O}(L)$), and the minimization of (20) with respect to the circumferential wave number q_y leads to the critical circumferential wavelength that is generally smaller than the circle circumference $2\pi R$ but always larger than the wavelength (19) in the axial compression case. Simple formulae for the critical circumferential stress and the critical wavelength ℓ_y can be obtained by considering a given axial wave number $q_x = \mathcal{O}(1/L)$ that is smaller than the circumferential wave number q_y. With these simplifications, Eq. (20) can be written as

$$h_f|\sigma_y^c| = Dq_y^2 + \frac{E_f h_f}{R^2}\frac{q_x^4}{q_y^6}, \tag{21}$$

and the minimization with respect to q_y is quite straightforward:

$$\begin{cases} q_y = \left[36\left(1-\nu^2\right)\right]^{1/8}\dfrac{q_x^{1/2}}{\left(Rh_f\right)^{1/4}} \Longrightarrow \ell_y = \dfrac{2\pi}{q_y} = \mathcal{O}\left[L^{1/2}\left(Rh_f\right)^{1/4}\right], \\ |\sigma_y^c| = \dfrac{4}{[36(1-\nu^2)]^{3/4}}\dfrac{E_f h_f^{3/2} q_x}{R^{1/2}}. \end{cases} \tag{22}$$

Therefore, this simple and classical buckling analysis predicts buckling patterns under lateral pressure loading that are quite different from those found in axial compression case. The circumferential wavelength ℓ_y turns out to be smaller than the axial one ($L^{1/2}(Rh_f)^{1/4} \ll L$), and the critical stress is generally much smaller than in the axial compression case ($h_f^{3/2} q_x / R^{1/2} \ll h_f/R$). This study will be continued to account for the effects of the core stiffness and boundary conditions.

3.3. A simplified analysis for pressure-type buckling

In reality, the solutions of the nonlinear problems are not always harmonics so that the previous analysis can be only qualitative. Nevertheless, relatively simple critical and post-buckling solutions are available (Abdelmoula et al., 1992; Abdelmoula and Leger, 2008) based on the observation that the circumferential wavelength is much smaller than the cylindrical length. In this paper, this simplified approach is extended to core-shells governed by system (11). First, to distinguish the tangent operator at the bifurcation point and the nonlinear part, we modify Eq. (11) by introducing the additional stress function $f(x, y) =$

$F(x,y) - \frac{1}{2}\left(\sigma_y^0 x^2 + \sigma_x^0 y^2\right)$:

$$\begin{cases} D\Delta^2 w - \dfrac{1}{R}\dfrac{\partial^2 f}{\partial x^2} - h_f\left(\sigma_x^0 \dfrac{\partial^2 w}{\partial x^2} + \sigma_y^0 \dfrac{\partial^2 w}{\partial y^2}\right) + K_s w - [f,w] = 0, \\ \dfrac{1}{E_f h_f}\Delta^2 f + \dfrac{1}{R}\dfrac{\partial^2 w}{\partial x^2} + \dfrac{1}{2}[w,w] = 0. \end{cases} \tag{23}$$

As shown in Fig. 2, thermal or pressure loading generally leads to the churro-like mode that is characterized by faster variations in the circumferential direction. This feature is the starting point of a simplified approach established in Abdelmoula et al. (1992); Abdelmoula and Leger (2008). It consists in neglecting all the axial derivatives ($\partial/\partial x \ll \partial/\partial y$), except for the coupling terms $(1/R)(\partial^2/\partial x^2)$ due to the crucial role of the curvature in any shell buckling problem, as well as the nonlinear terms [*f, w*] and [*w, w*] that contain the same number of derivatives in both directions. This leads to a simplified system:

$$\begin{cases} D\dfrac{\partial^4 w}{\partial y^4} - \dfrac{1}{R}\dfrac{\partial^2 f}{\partial x^2} - h_f\sigma_y^0\dfrac{\partial^2 w}{\partial y^2} + K_s w - [f,w] = 0, \\ \dfrac{1}{E_f h_f}\dfrac{\partial^4 f}{\partial y^4} + \dfrac{1}{R}\dfrac{\partial^2 w}{\partial x^2} + \dfrac{1}{2}[w,w] = 0. \end{cases} \tag{24}$$

In Abdelmoula and Leger (2008), this simplified model has been validated by an asymptotic expansion with respect to a small parameter related to the Batdorf parameter, *i.e.* $1/\sqrt{Z} \approx \sqrt{Rh_f}/L$. Each equation in (24) is reduced to the second order with respect to $\partial/\partial x$ from the starting model (23) that is of the fourth order. This feature means that the solution of the initial system (23) involves boundary layers that have consequences on boundary conditions to be associated with the simplified system (24).

3.4. Dimensional analysis

We now seek the parameters influencing the buckling behavior of core-shell cylindrical systems under thermal loading. The investigation is based on the simplified model (24), knowing that the transition between the simplified system (24) and the initial one (23) is governed by the Batdorf parameter. Generally, within nonlinear shell/plate theory, the deflection is assumed to be of the order of the shell/plate thickness. According to the previous discussion, the characteristic lengths are the structural length L in the axial direction and the half wavelength ℓ_w in the circumferential direction. But this half buckling wavelength ℓ_w is unknown and is involved in the definition of the Winkler foundation stiffness K_s, as seen in Eq. (10). Nevertheless, the order of its magnitude is known so that we can scale the circumferential variable "y" by another length L_y that is of the same order of magnitude as ℓ_w. This leads to the following similitude assumptions:

$$w = h_f\bar{w}, \quad x = L\bar{x}, \quad y = L_y\bar{y}, \quad f = D\bar{f}, \quad L_y = L^{1/2}\left(Rh_f\right)^{1/4}. \tag{25}$$

Next one has to replace the unknown wavelength by dimensionless quantities and we propose the number of circumferential periods "n" that is an integer or the wave number $\bar{q}$ associated with the dimensionless variable $\bar{y}$. They are connected by

$$\frac{\pi}{\ell_w} = \frac{\bar{q}}{L_y} = \frac{n}{R}. \tag{26}$$

By substituting Eq. (25) into Eq. (24) and accounting for Eqs. (10) and (26), one obtains

$$\begin{cases} \dfrac{\partial^4 \bar{w}}{\partial \bar{y}^4} - \dfrac{\partial^2 \bar{f}}{\partial \bar{x}^2} - \Sigma\dfrac{\partial^2 \bar{w}}{\partial \bar{y}^2} + \bar{q}C_t^*\bar{w} - \left(\dfrac{Rh_f}{L^2}\right)^{1/2}\left[\bar{f},\bar{w}\right] = 0, \\ \dfrac{1}{12(1-\nu_f^2)}\dfrac{\partial^4 \bar{f}}{\partial \bar{y}^4} + \dfrac{\partial^2 \bar{w}}{\partial \bar{x}^2} + \dfrac{1}{2}\left(\dfrac{Rh_f}{L^2}\right)^{1/2}[\bar{w},\bar{w}] = 0, \end{cases} \tag{27}$$

where the bracket operator is defined in (8), but with respect to the scaled dimensionless variables $(\bar{x},\bar{y})$. Four dimensionless parameters appear in (27). The first one is Poisson's ratio ν_f of the shell, whose influence should be rather limited. The second one, $\Sigma = \sigma_y^0 h_f L_y^2/D \Longleftrightarrow \sigma_y^0 = E_f h_f^{3/2}\Sigma/[12(1-\nu_f^2)LR^{1/2}]$, is the dimensionless loading parameter, *i.e.* the bifurcation parameter that varies to study the response of the system. The third one combines the modulus ratio and the structural geometry involving curvature:

$$\begin{cases} C_t^* = \dfrac{24(1-\nu_f^2)}{(3-\nu_s)(1+\nu_s)}C_t, \\ C_t = \dfrac{E_s}{E_f}\left(\dfrac{L_y}{h_f}\right)^3 = \dfrac{E_s}{E_f}\left(\dfrac{L}{h_f}\right)^{3/2}\left(\dfrac{R}{h_f}\right)^{3/4}. \end{cases} \tag{28}$$

This ratio C_t or C_t^* is the main characteristic dimensionless parameter of the core-shell cylindrical system, which implies the influence of the core stiffness with respect to the shell stiffness. It differs from the parameter C_s introduced in Xu and Potier-Ferry (2016b) since the instability modes are quite different between external pressure and axial compression. The last parameter $(Rh_f/L^2)^{1/2}$ in Eq. (27) recovers the Batdorf parameter, but one will see that it can be dropped as it appears just before the two quadratic terms. Through re-scaling the unknowns of system (27) by

$$\bar{w} = w^*/\eta, \quad \bar{x} = x^*, \quad \bar{y} = y^*, \quad f = f^*/\eta, \quad \eta = \left(Rh_f/L^2\right)^{1/2}, \tag{29}$$

one gets a new version of the model as

$$\begin{cases} \dfrac{\partial^4 w^*}{\partial y^{*4}} - \dfrac{\partial^2 f^*}{\partial x^{*2}} - \Sigma\dfrac{\partial^2 w^*}{\partial y^{*2}} + \bar{q}C_t^* w^* - [f^*,w^*] = 0, \\ \dfrac{1}{12(1-\nu_f^2)}\dfrac{\partial^4 f^*}{\partial y^{*4}} + \dfrac{\partial^2 w^*}{\partial x^{*2}} + \dfrac{1}{2}[w^*,w^*] = 0. \end{cases} \tag{30}$$

Thus, in what follows, the behavior of the system will be discussed as a function of the parameter C_t^* defined in (28).

3.5. Boundary layers and boundary conditions

The presence of boundary layers is one of the main features of the buckling of cylindrical shells under circumferential compression ($\sigma_y < 0$). As theoretically explained in Abdelmoula and Leger (2008), these boundary layers are associated with large values of the Batdorf parameter $Z = L^2\sqrt{1-\nu_f^2}/(Rh_f)$, *i.e.* $Z \geq 100$, which is generally the case for thin shell buckling. The rapid variations in boundary regions have consequences for the boundary conditions to be applied to the simplified model (24). To illustrate this statement, let us consider full finite element computations of core-shell cylinders under thermal loading for two cases with the same Batdorf parameter $Z = 954$ but with different dimensionless parameters $C_t = 0.0056$ and $C_t = 266$, respectively. Fig. 4 illustrates the axial profile of the deflection $x \to w(x, 0)$ and its derivative around the first bifurcation to be representative of bifurcation modes. It shows a rapid variation of the slope $w_{,x}$ close to the boundary, which satisfies the clamped condition $w_{,x} = 0$. In fact, it clearly appears that a smooth extrapolation of the slope $w_{,x}$ up to the boundary would satisfy $w_{,xx} = 0$ but not $w_{,x} = 0$. This boundary

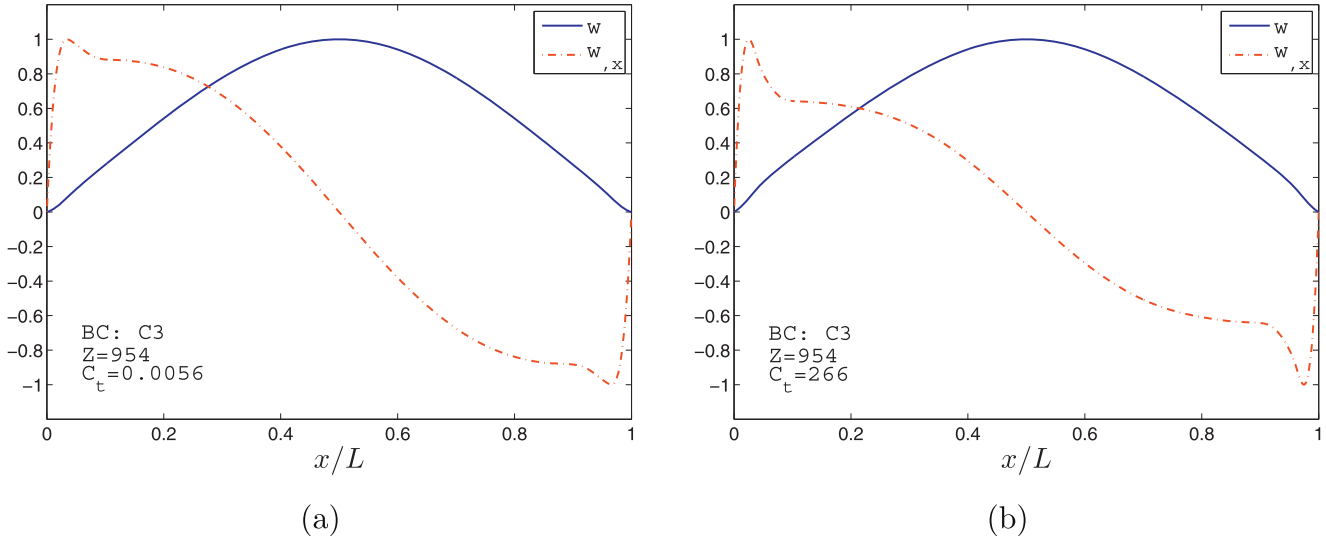

Fig. 4. Buckling modes and the corresponding rotations obtained by the numerical model in Section 2 with boundary condition **C**3 and Batdorf parameter $Z = 954$: (a) $C_t = 0.0056$; (b) $C_t = 266$. The size of the boundary layers remains the same since the same Batdorf parameter is taken into account.

Table 1
Boundary conditions (BCs) imposed on models.

BCs for initial problem (7)	BCs for simplified problem (24)
C1, **C**2, **S**1, **S**2 ($u = w = 0$)	$w = w_{,x} = 0$
C3, **C**4, **S**3, **S**4 ($N_x = w = 0$)	$w = w_{,xx} = 0$

condition $w_{,xx} = 0$ is the one to be imposed on the simplified model (24) that disregards the boundary layers. Roughly, this is a consequence of boundary conditions on the axial force N_x and it follows the linear version of Eq. (24b):

$$N_x = 0 \Longrightarrow \frac{\partial^2 f}{\partial y^2} = 0 \overset{\text{cf.}(24-b)}{\Longrightarrow} \frac{\partial^2 w}{\partial x^2} = 0. \tag{31}$$

A rigorous explanation accounting for boundary layers is given in Abdelmoula and Leger (2008) as well as a treatment of the case $u = 0$. It was theoretically found that the width of boundary layers is related to the Batdorf parameter and satisfies $\mathcal{O}(1/\sqrt{Z})$. Indeed, boundary layers shown in Fig. 4 have the same size. These results for the boundary conditions associated with the model (24) are summarized in Table 1. Note that only the axial boundary ($u = 0$ or $N_x = 0$) has a strong effect on the bifurcation load, which was early recognized by Sobel (1964). The other boundary conditions ($v = 0$ or $N_{xy} = 0$, $w_{,x}$ or $w_{,xx} = 0$) offer a minor influence and act only on the boundary layers. Of course the persistence of these conclusions in the post-buckling regime and in the presence of the core can be re-discussed.

3.6. Bifurcation analysis

Bifurcation loads are obtained from the linearized version of the dimensionless system (30). For simplicity, we omit the superscripts stars. The bifurcation modes are assumed in a harmonic form along the circumferential direction:

$$\begin{cases} w(x,y) = \hat{w}(x)\cos(qy), \\ f(x,y) = \hat{f}(x)\cos(qy). \end{cases} \tag{32}$$

Hence, the modes in the axial direction are the solutions of an ordinary differential system obtained from the linear version of (30):

$$\begin{cases} \left(q^4 + \Sigma q^2 + qC_t^*\right)\hat{w} - \dfrac{\mathrm{d}^2\hat{f}}{\mathrm{d}x^2} = 0, \\ \dfrac{q^4}{12(1-\nu_f^2)}\hat{f} + \dfrac{\mathrm{d}^2\hat{w}}{\mathrm{d}x^2} = 0. \end{cases} \tag{33}$$

Through eliminating the stress function $\hat{f}$, one finds a deflection determined by a fourth-order differential equation:

$$12\left(1-\nu_f^2\right)\frac{\mathrm{d}^4\hat{w}}{\mathrm{d}x^4} + \left(q^8 + \Sigma q^6 + q^5 C_t^*\right)\hat{w} = 0. \tag{34}$$

This eigenvalue problem is well known (*e.g.* vibration modes of a beam) and it has been associated with buckling under external pressure in Abdelmoula and Leger (2008). Let us recall the smallest eigenpair for $x \in [-1/2, 1/2]$. In the case without axial force ($N_x = w = w_{,xx} = 0$), the solution reads ($\Sigma < 0$):

$$\begin{cases} \hat{w}(x) = \cos(\pi x), \\ |\Sigma(q)| = q^2 + \dfrac{12(1-\nu_f^2)\pi^4}{q^6} + \dfrac{C_t^*}{q}, \end{cases} \tag{35}$$

or in the case where the axial displacement u is locked on the boundary ($u = w = w_{,x} = 0$):

$$\begin{cases} \hat{w}(x) = A\cos(\pi\rho x) + B\cosh(\pi\rho x), \\ |\Sigma(q)| = q^2 + \dfrac{12(1-\nu_f^2)\rho^4\pi^4}{q^6} + \dfrac{C_t^*}{q}, \end{cases} \tag{36}$$

where A and B are constants and $\rho \approx 1.5056$ is the smallest root of $\tan(\pi\rho/2) + \tanh(\pi\rho/2) = 0$. As underlined in Karam and Gibson (1995), the minimization of (35-b) or (36-b) with respect to q is difficult since this leads to an eighth-order polynomial equation. Nevertheless, it is clear that the critical stress (minimum of $\Sigma(q)$) depends only on two dimensionless parameters, *i.e.* Poisson's ratio ν_f of the shell and the dimensionless parameter C_t^*. The numerical minimization is quite straightforward as the possible values of the wave number are discrete ($q = nL_y/R$) (see Fig. 5).

The values of the critical stress Σ_{cr} and the associated wave number q_{cr} are presented in Table 2 as a function of the core stiffness parameter C_t^* in the case of $\nu_f = 0.4$. These results correspond to exact solutions of the simplified model (24) but not to the full model (7). As expected, the wave number and the critical stress increase with the rise of core stiffness C_t^*. Two groups of boundary conditions defined in Table 1 are considered. For a very soft

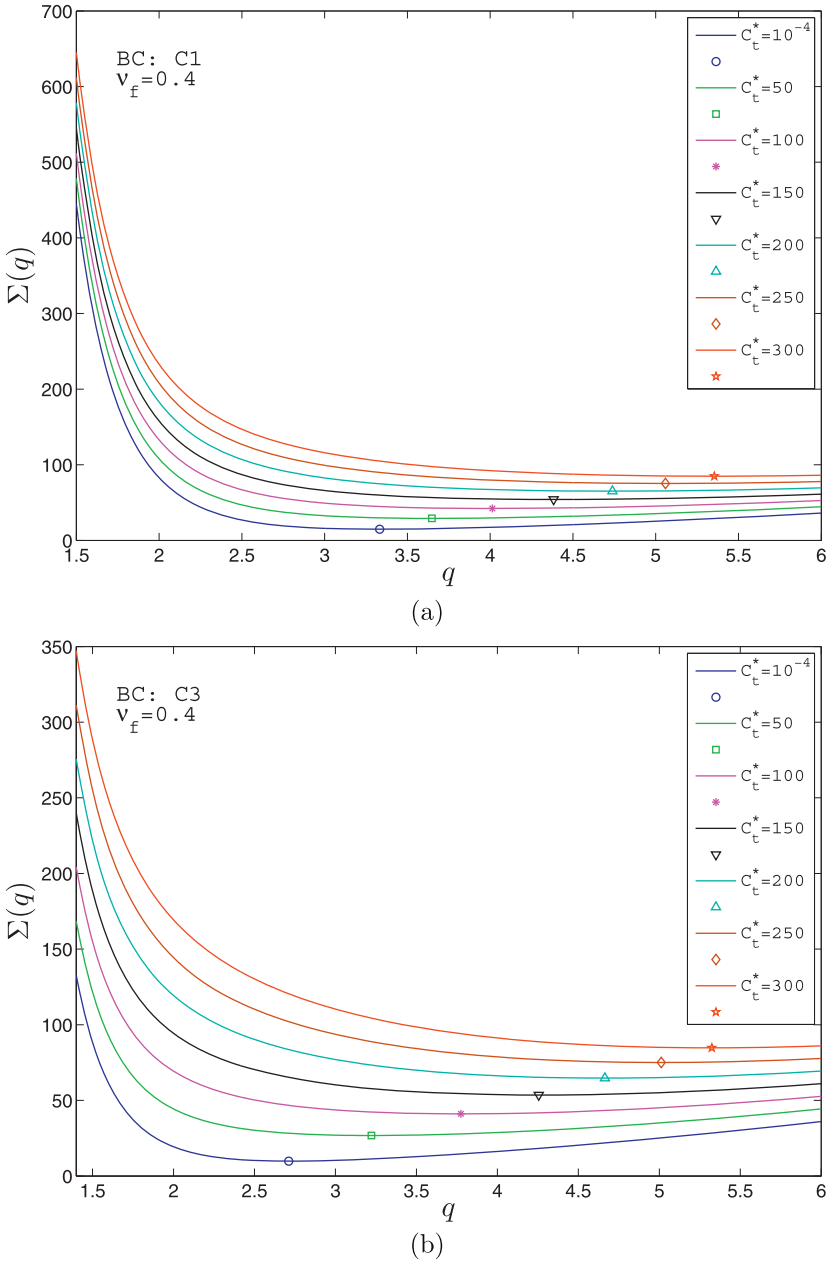

Fig. 5. The load $\Sigma(q)$ in function of the wave number q. The markers stand for the critical load and its associated wave number. (a) boundary condition **C**1; (b) boundary condition **C**3.

Table 2
Critical stress Σ_{cr} and wave number q_{cr} with boundary conditions **C**1 and **C**3.

	$C_t^*=10^{-4}$	$C_t^*=1$	$C_t^*=10$	$C_t^*=30$	$C_t^*=50$	$C_t^*=100$	$C_t^*=200$	$C_t^*=300$
$q_{cr}^{\mathbf{C1}}$	3.33	3.34	3.39	3.51	3.65	4.01	4.74	5.35
$\Sigma_{cr}^{\mathbf{C1}}$	14.79	15.09	17.77	23.57	29.15	42.23	65.11	84.91
$q_{cr}^{\mathbf{C3}}$	2.71	2.72	2.80	3.00	3.22	3.78	4.66	5.32
$\Sigma_{cr}^{\mathbf{C3}}$	9.82	10.19	13.45	20.35	26.78	41.08	64.73	84.74
$\Sigma_{cr}^{\mathbf{C1}}/\Sigma_{cr}^{\mathbf{C3}}$	1.51	1.48	1.32	1.16	1.09	1.03	1.01	1.00

core, the critical stress for a full clamped case **C**1 is 1.5 times larger than that in the case **C**3 with $N_x = 0$, which agrees well with the solutions in Sobel (1964); Abdelmoula and Leger (2008) for a pure shell structure. This additional buckling strength due to the boundary condition $u = 0$ exists for a core-shell cylinder as well, but the ratio $\Sigma_{cr}^{\mathbf{C1}}/\Sigma_{cr}^{\mathbf{C3}}$ decreases with the increase of C_t^* and tends to be one for a relatively stiff core so that the buckling strength is almost insensitive to BCs when $C_t^* \geqslant 100$.

3.7. Post-bifurcation analysis

The post-bifurcation behavior is a key result for core-shell cylinders subjected to axial compression, and the post-buckling re-

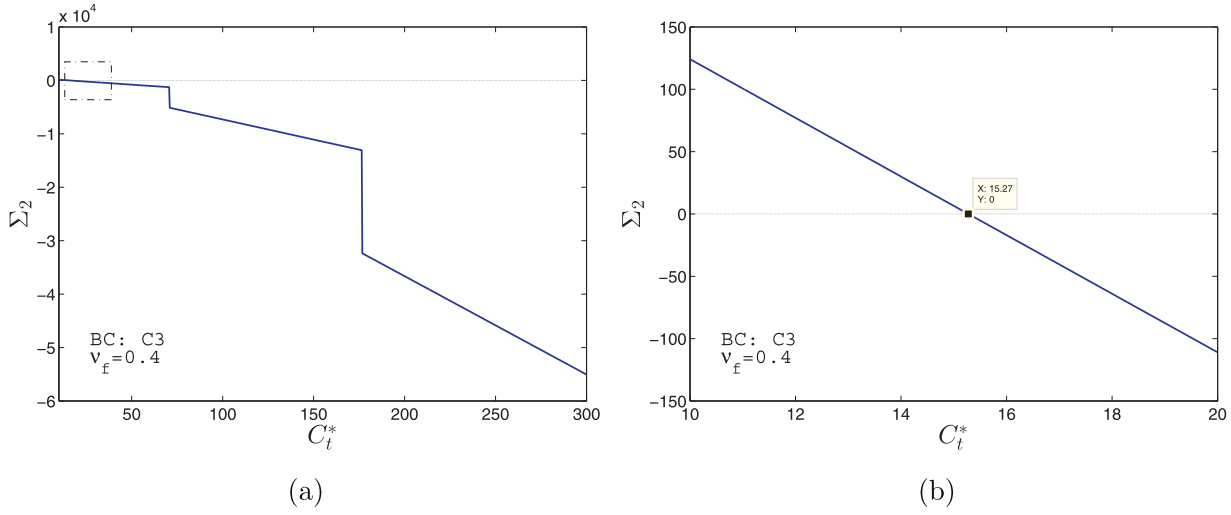

Fig. 6. Σ_2 in function of C_t^* with boundary condition **C**3 and $\nu_f = 0.4$. The sign of Σ_2 changes at $C_t^* = 15.27$. (b) zoom of (a).

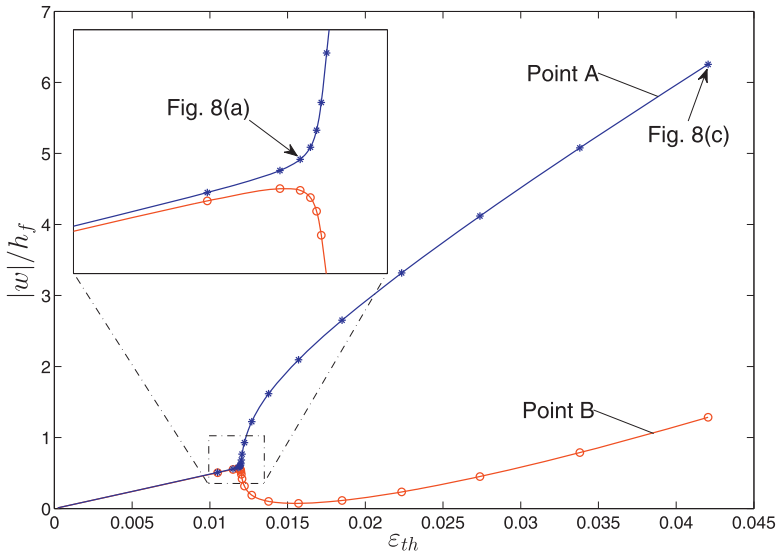

Fig. 7. Bifurcation diagram of Core-shell I with $C_t = 266$, $Z = 2113$ and boundary condition **C**1. The points A and B are marked in Fig. 3. Representative wrinkling shapes in Fig. 8 on the post-buckling evolution path are marked. ANM parameters: $n = 15$, $\delta = 10^{-4}$, 18 steps. Each point corresponds to one ANM step.

sponse is usually unstable with a soft core and tends to be stable with a stiff core (Zhao et al., 2014; Xu and Potier-Ferry, 2016b). A post-critical bifurcation is not common for a curved shell and thus the characteristics of stiff core-shells seem highly interesting. The bifurcation theory (Budiansky, 1974; Koiter, 1945; 2009) allows distinguishing between subcritical and supercritical post-bifurcation according to the sign of a number, named Σ_2 in this paper. The nonlinear system (30) has a simple structure involving linear and quadratic operators:

$$\mathcal{L}(\mathbf{U}) + (\Sigma - \Sigma_0)\mathcal{L}'(\mathbf{U}) = Q(\mathbf{U}, \mathbf{U}), \tag{37}$$

where the linear operators $\mathcal{L}(\mathbf{U})$ and $\mathcal{L}'(\mathbf{U})$ are self-adjoint and the first one is singular, *i.e.* $\exists \mathbf{U}_1 \neq 0$ such that $\mathcal{L}(\mathbf{U}_1) = 0$. Classical asymptotic expansions of the bifurcating curve emanating from the bifurcation point (the standard case of a symmetric bifurcation) can be written as

$$\begin{cases} \mathbf{U} = a\mathbf{U}_1 + a^2\mathbf{U}_2 + a^3\mathbf{U}_3 + \dots, \\ \Sigma - \Sigma_0 = a^2\Sigma_2 + a^4\Sigma_4 + \dots. \end{cases} \tag{38}$$

The bifurcation curve exists beyond the bifurcation point if the two terms Σ_2 and Σ_0 have the same sign. Here Σ_0 is negative so that the bifurcation is either supercritical and stable if $\Sigma_2 < 0$, or subcritical and unstable if $\Sigma_2 > 0$. The identification of the powers of the path parameter "a" gives a sequence of equations:

$$\begin{cases} \mathcal{L}(\mathbf{U}_1) = 0, \\ \mathcal{L}(\mathbf{U}_2) = Q(\mathbf{U}_1, \mathbf{U}_1), \\ \mathcal{L}(\mathbf{U}_3) + \Sigma_2\mathcal{L}'(\mathbf{U}_1) = 2Q(\mathbf{U}_1, \mathbf{U}_2). \end{cases} \tag{39}$$

One does not need to solve the last equation in (39), but only writes a solvability condition by taking the scalar product of (39-c) with the kernel $\mathbf{U}_1$ of the linear operator $\mathcal{L}$:

$$\Sigma_2 = \frac{2\langle Q(\mathbf{U}_1, \mathbf{U}_2), \mathbf{U}_1\rangle}{\langle \mathcal{L}'(\mathbf{U}_1), \mathbf{U}_1\rangle}. \tag{40}$$

The analytical calculation of Σ_2 is straightforward and more details are presented in Appendix A. The value of Σ_2 has been computed as a function of the dimensionless parameter C_t^*, from Eqs. (39), (40) and (55)–(60) in Appendix A, and with the aid of symbolic code in Mathematica (Wolfram, 1991). The results are reported in the case of boundary conditions $\mathbf{C}3 - \mathbf{C}4 - \mathbf{S}3 - \mathbf{S}4$ and $\nu_f = 0.4$, as shown in Fig. 6. For a small value of C_t^*, Σ_2 is positive, which is in good agreement with the well-known unstable post-buckling

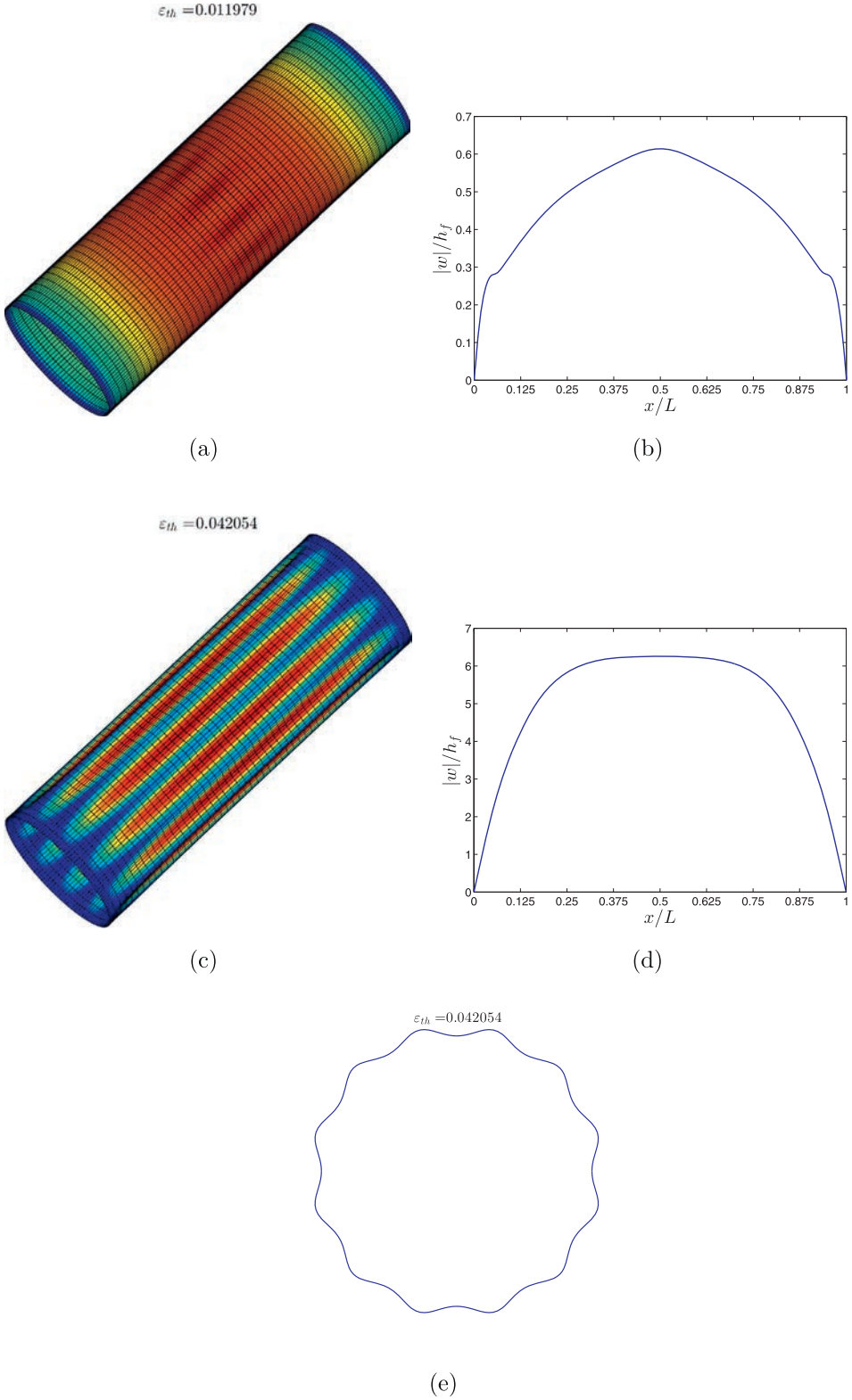

Fig. 8. The left column shows two representative wrinkling patterns of Core-shell I with $C_t = 266$, $Z = 2113$ and boundary condition **C**1, when the load increases. The color contour represents w/h_f. The right column presents the associated instability modes along the length. (e) cross-section contour at $x = L/2$ at the final loading step, with wave number $n = 12$.

behavior of a pure shell without a core under lateral or external pressure (Yamaki, 1984). The sign of Σ_2 changes to be negative for $C_t^* = 15.27$ and decreases significantly with the increase of C_t^*, which indicates a strongly supercritical post-buckling behavior in the presence of rather stiff core. Note that discontinuities in Fig. 6a are due to the change of circumferential wave number "n". Thus one recovers the same features as in axial compression: an unstable post-buckling response for a soft core that turns out to be stable for a sufficiently stiff core. These results will be re-discussed in what follows from finite element calculations.

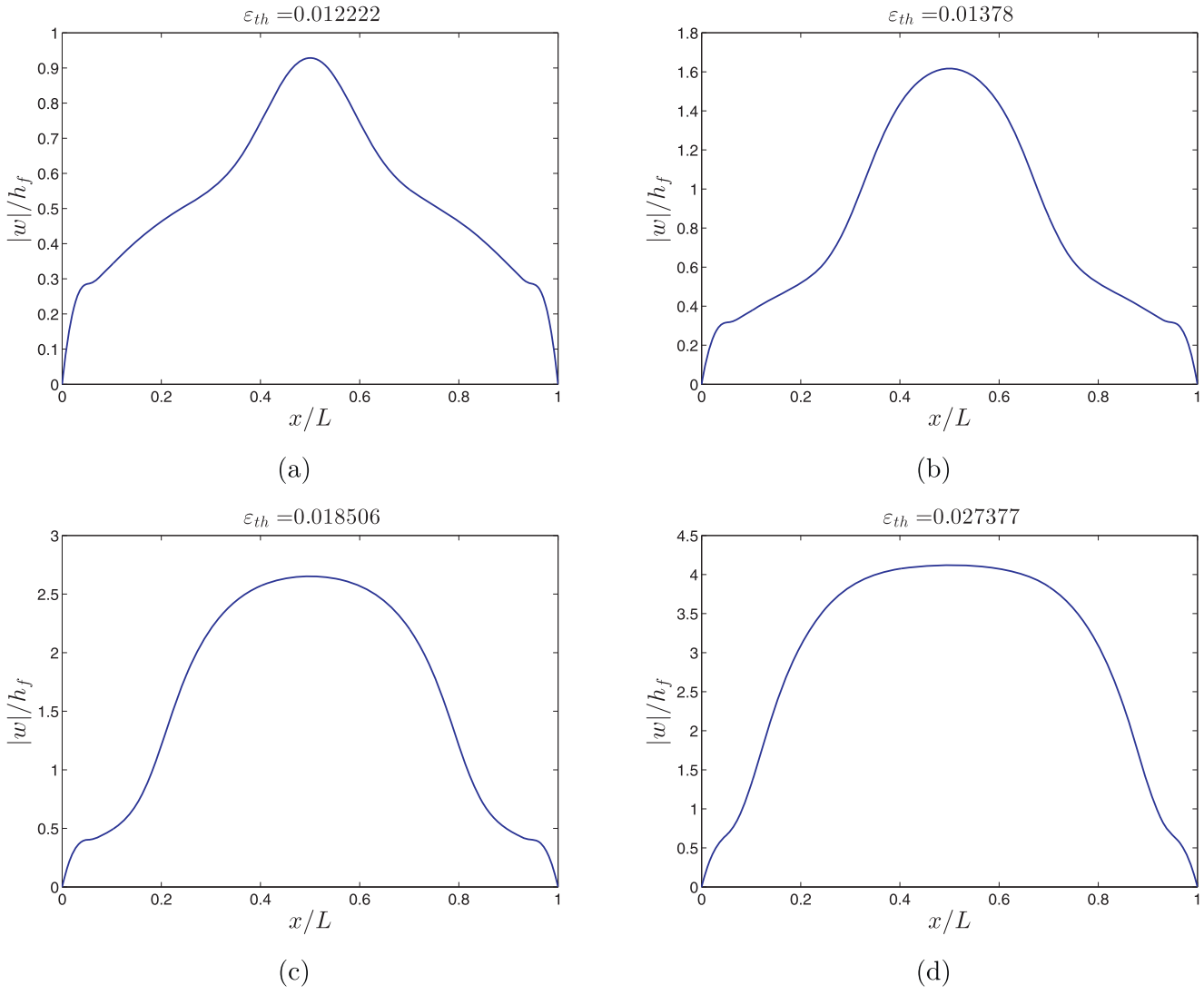

Fig. 9. The post-buckling evolution of boundary layers beyond bifurcation of Core-shell I with $C_t = 266$, $Z = 2113$ and boundary condition **C**1, when the load increases. The boundary layers affect the bulk response that becomes more flattened for larger values of the thermal load.

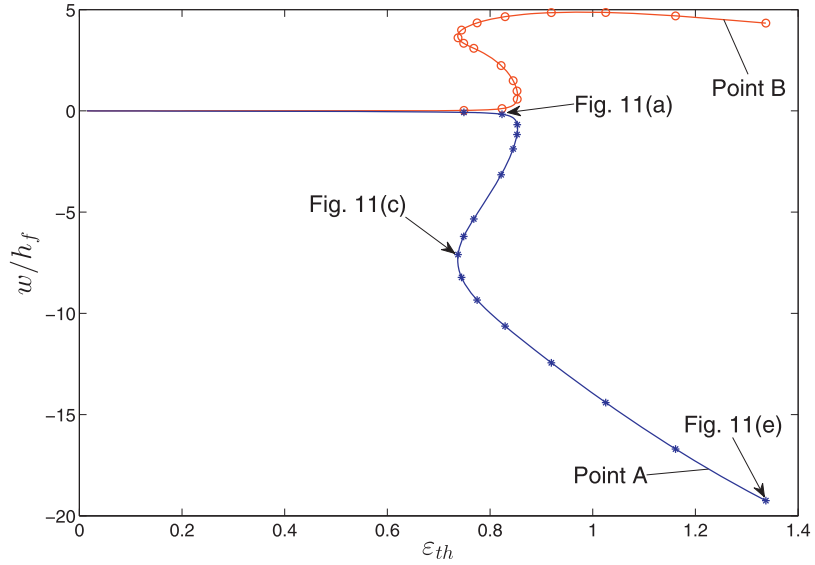

Fig. 10. Bifurcation diagram of Core-shell II with $C_t = 0.1$, $Z = 2113$ and boundary condition **C**1. The points A and B are marked in Fig. 3. Representative wrinkling shapes in Fig. 11 on the post-buckling evolution path are marked. ANM parameters: $n = 15$, $\delta = 10^{-4}$, 16 steps. Each point corresponds to one ANM step.

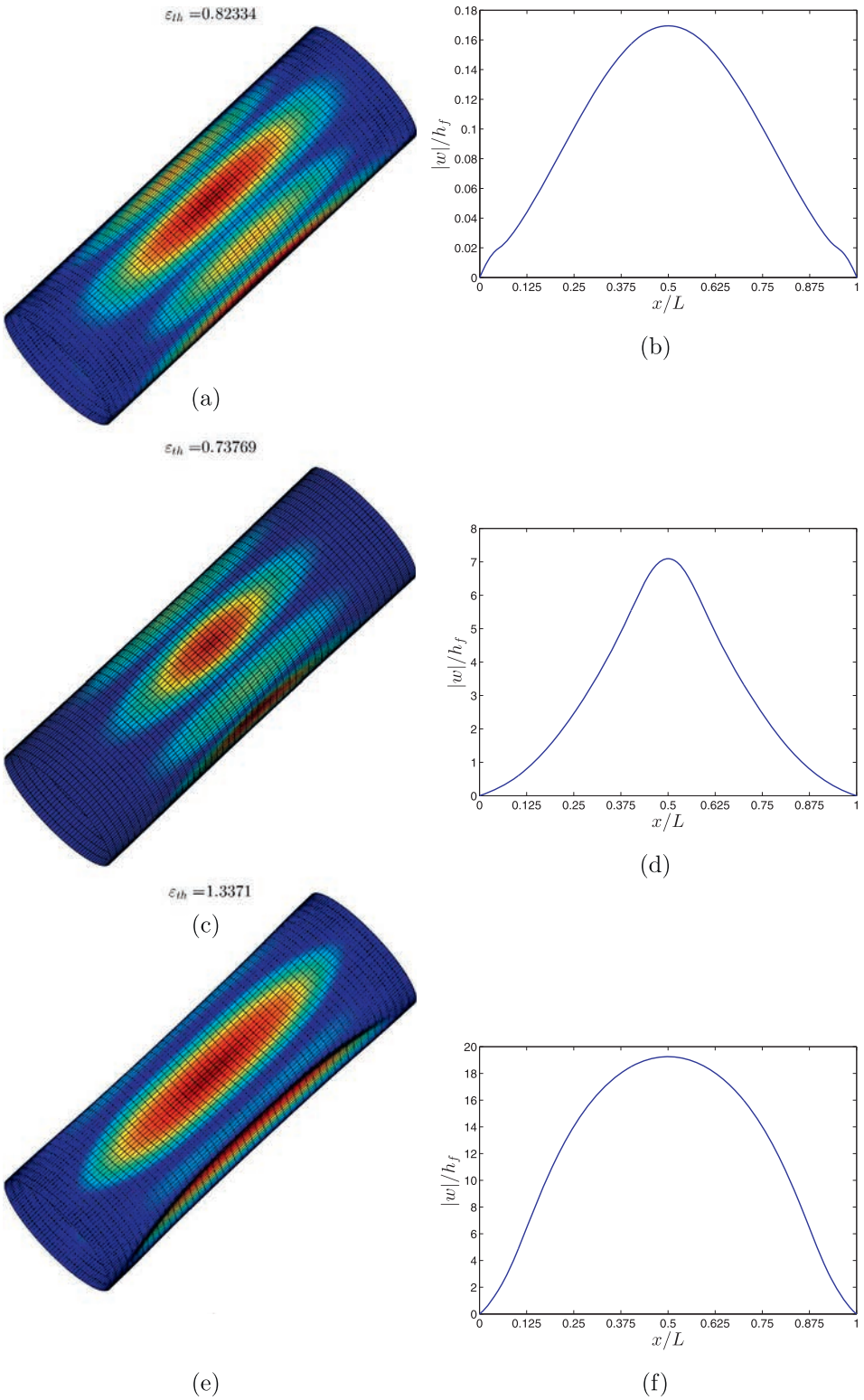

Fig. 11. The left column shows a sequence of representative wrinkling patterns of Core-shell II with $C_t = 0.1$, $Z = 2113$ and boundary condition **C**1. The color contour denotes w/h_f. The right column presents the associated instability modes along the length.

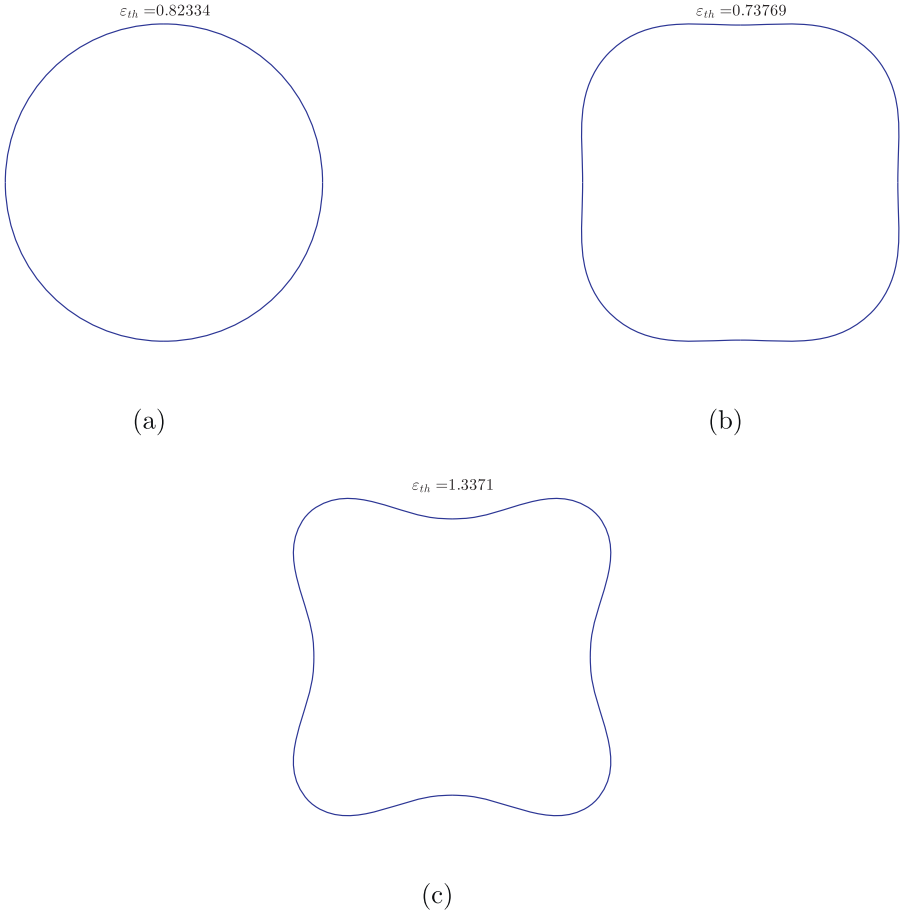

Fig. 12. A shape evolution of cross-section ($x = L/2$) of Core-shell II with $C_t = 0.1$, $Z = 2113$ and boundary condition **C1**. Wave number $n = 4$ at the final step.

Table 3
Material and geometric properties of various core-shell cylindrical structures.

Core-shell	E_f (MPa)	E_s (MPa)	ν_f	ν_s	h_f (mm)	R (mm)	L (mm)	C_t	C_t^*	Z	n_{cr}
I	1.3×10^3	1.8	0.4	0.48	10^{-3}	69.4×10^{-3}	0.4	266	1438	2113	11
II	3.45×10^6	1.8	0.4	0.48	10^{-3}	69.4×10^{-3}	0.4	0.1	0.5	2113	4
III	2.16×10^4	1.8	0.4	0.48	10^{-3}	91.0×10^{-3}	0.1	2.5	13.5	101	8
IV	2.16×10^4	1.8	0.4	0.48	10^{-3}	32.0×10^{-3}	0.2	3.2	17.3	1146	3
V	2.16×10^4	1.8	0.4	0.48	10^{-3}	94.0×10^{-3}	0.1	2.5	13.5	98	10
VI	2.16×10^4	1.8	0.4	0.48	10^{-3}	28.0×10^{-3}	0.2	2.9	15.7	1309	3
VII	1.3×10^3	5.1	0.4	0.48	10^{-3}	69.4×10^{-3}	0.2	266	1438	528	16

4. Results and discussion

4.1. Computational methodology

The nonlinear post-buckling of core-shell cylindrical structures subjected to thermal loading will be investigated numerically by considering shell elements for the surface layer and solid elements for the core, as presented in Section 2. The following computational technique has been chosen to avoid most restrictive assumptions on initial geometric imperfections that are generally performed in the literature (Zhao et al., 2014; Jia et al., 2015): the considered domain herein is three-dimensional without geometric imperfection and path-following technique provides the post-buckling response of the system beyond the primary bifurcation (Xu and Potier-Ferry, 2016b).

Material and geometric properties of core-shell composite systems are shown in Table 3. According to the dimensional analysis performed in Section 3.4, the two key parameters to determine buckling response are core stiffness parameter C_t and the Batdorf parameter Z, which are in function of geometric and physical constants: radius/thickness ratio R/h_f, length/thickness ratio L/h_f and modulus ratio E_f/E_s. Hence, various cases with representative geometric and material properties are considered for the calculations: some of them have a relatively big C_t or Z while the others may hold a small value (see Table 3). Poisson's ratio is a dimensionless measure of the degree of compressibility. Compliant materials for the core, such as elastomers, are nearly incompressible with $\nu_s = 0.48$. In this paper, thermal load is applied to the core whereas the shell is load free, as formulated in Section 2. In order to trigger a transition from the fundamental to the bifurcated branch, a small perturbation force, $f_z = 10^{-6}$, is imposed on the shell. Introduction of such small perturbation forces is a common technique for solving bifurcation problems by continuation techniques (Doedel, 1981; Allgower and Georg, 1990), even when using commercial finite element codes. This artifice could be avoided by applying a specific procedure to compute the bifurcation branch

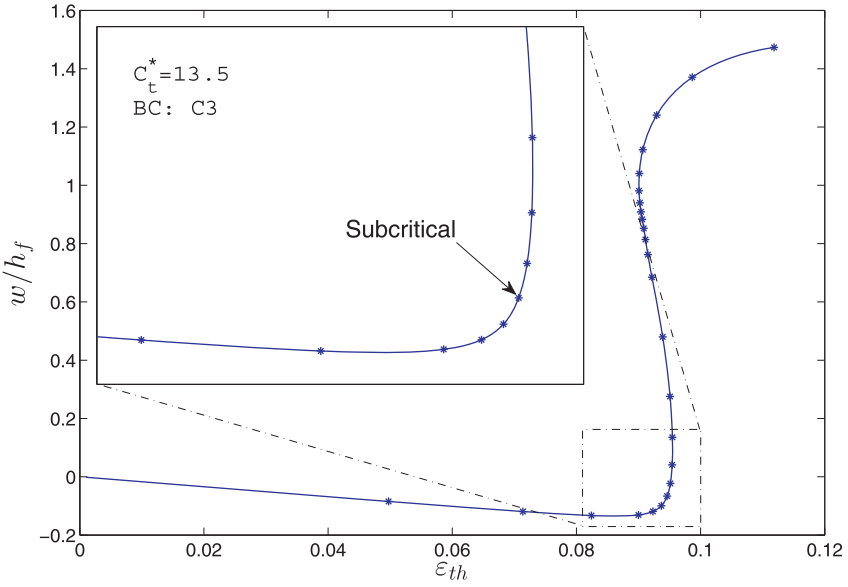

(a)

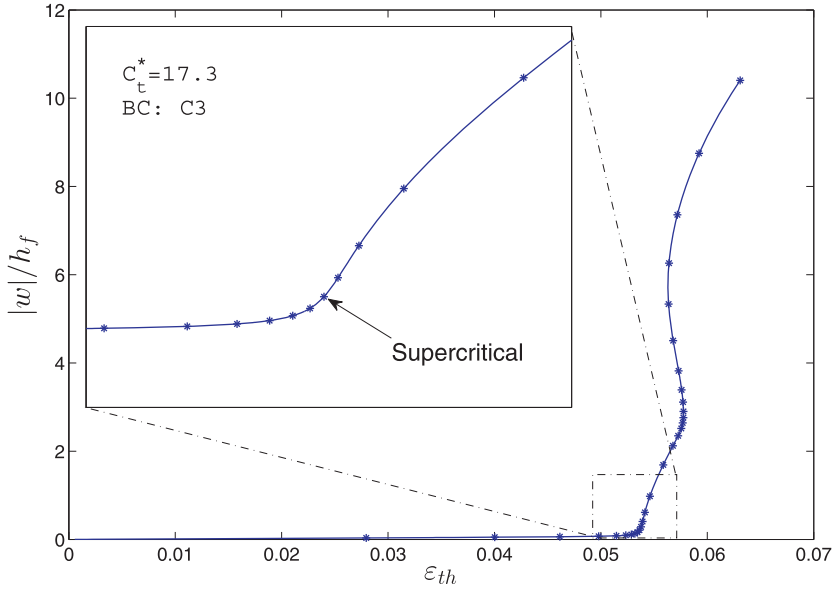

(b)

Fig. 13. Comparison of bifurcation diagrams between (a) Core-shell III with $C_t^* = 13.5$ and (b) Core-shell IV with $C_t^* = 17.3$. The boundary condition **C**3 is applied. ANM parameters: $n = 15$, $\delta = 10^{-6}$. Each point corresponds to one ANM step.

as in Boutyour et al. (2004); Vannucci et al. (1998). In this paper, the perturbation force f_z allows computing the whole bifurcated branch with a single continuation algorithm. The number of elements required for a convergent solution was carefully examined. Bifurcation points are detected by the criterion of small step accumulation. Indeed, when the starting point of a step is close to bifurcation, the radius of convergence of Taylor series coincides with the distance to the singular point, which explains that the continuation process 'knocks' against the bifurcation (Baguet and Cochelin, 2003). More advanced techniques are available for bifurcation detection such as bifurcation indicator (Xu et al., 2014; 2015b) and power series analysis (Cochelin and Medale, 2013), but the simple detection by sight will prove to be sufficient in our analyses. In what follows, we will explore the formation and evolution of several instability modes with different C_t and Z through the established model (5).

Due to geometric symmetry, only one quarter of the system is considered for the mesh for reduction of computational cost, and the corresponding symmetric boundary conditions on the circumferential edges are suitably applied. Consequently, the surface layer is meshed with 30×50 shell elements to ensure at least five elements within a single wave. The core is compatibly discretized by 7500 brick elements with five layers. Mesh convergence was carefully examined as in Xu and Potier-Ferry (2016b). Totally, the core-shell system contains 61,167 degrees of freedom (DOF) including the Lagrange multipliers. Note that some wrinkling modes and

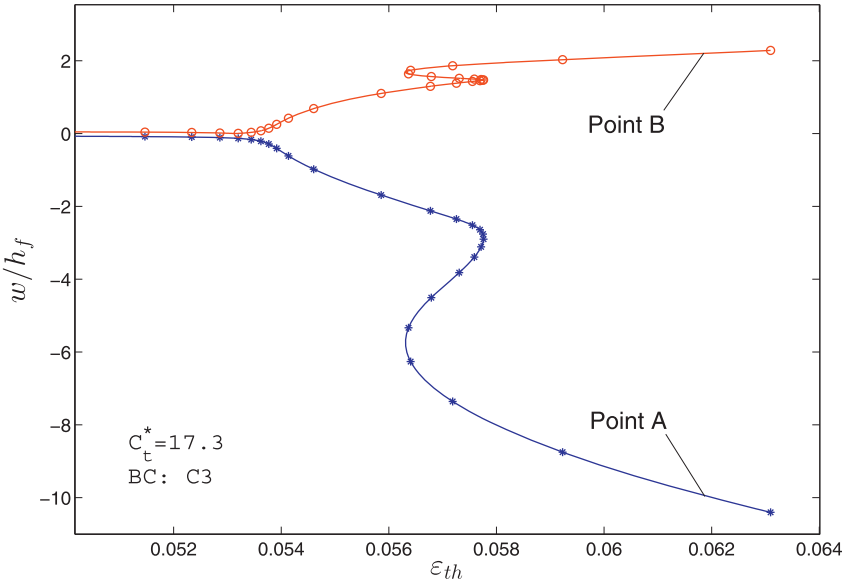

Fig. 14. Bifurcation curve of Core-shell IV with $C_t^* = 17.3$ and boundary condition **C**3. The points A and B are marked in Fig. 3.

mode interactions may be disregarded by considering only a part of the structure, especially the modes with an odd wave number "n".

4.2. Numerical results

Seven numerical tests presented in Table 3 will be discussed by considering two classical boundary conditions **C**1 and **C**3, cf. (12). Indeed, according to the simplified analysis in Section 3.5, there are two main classes of boundary conditions that are distinguished by the axial condition ($u = 0$ or $N_x = 0$), and the chosen boundary conditions are representatives of these two classes.

Let us begin with the cases with a relatively stiff core and soft core, respectively, which are characterized by the dimensionless ratio C_t: a large value $C_t = 266$ for the stiff core case and a small value $C_t = 0.1$ for the soft core one. The boundary condition (**C**1) and the Batdorf parameter ($Z = 2133$) are the same in these two tests. The bifurcation curves ($|w|/h_f$ *vs.* ε_{th}) are given in Figs. 7 and 10, respectively. There exists a single bifurcation point, while this bifurcation is supercritical for the stiff core case and subcritical for the soft core case, which was predicted by the analytical post-bifurcation analysis in Section 3.7 (the latter analysis was conducted for the other class of BCs). This subcritical/supercritical transition has also been observed in the case of axial compression (Xu and Potier-Ferry, 2016b) and is probably a characteristic feature for many core-shell buckling problems. The response with a hysteresis loop in the soft core case (see Fig. 10) is very close to the corresponding one in pure shell structures (Yamaki, 1984). Representative wrinkling patterns are illustrated in Figs. 8, 11 and 12, respectively. A churro-like buckling mode occurs at the bifurcation in the center of the core-shell system, with an axial profile similar to the prediction of the simplified approach in Section 3.6, see Eq. (36). Boundary layers appear clearly near the two ends of the system in the case of large Batdorf parameter (see Figs. 8b and 11 b), as discussed in Section 3.5. The boundary layer holds a relatively stable thickness in the post-bifurcation range, while it has a considerable effect on the bulk response that becomes more flattened for large values of the thermal load, as illustrated in Fig. 9. When the load increases, the churro-like pattern evolves and the boundary layers turn out to diminish. The computational wave number along the circumferential direction in Fig. 8e is counted by 12, which is very close to the analytical solution $n_{cr} = 11$ shown in Table 3. Note that $n = 11$ is not permitted due to geometric symmetry consideration in finite element calculations. In the soft core case with $C_t = 0.1$, the numerical wave number $n = 4$ (see Fig. 12) coincides with the analytical prediction in Table 3.

The load-displacement curves in Figs. 7 and 10 are depicted in terms of the applied thermal strain ε_{th} in the core. The connection between this strain and the circumferential stress σ^f in the shell is not apparent in general, while it can be established analytically in the pre-buckling stage if one assumes a uniform and isotropic stress field in the core, as seen in Eq. (64) in Appendix B. For a very soft core ($E_s/E_f \ll h_f/R$), the compressive stress can be approximated by $\sigma^f \approx E_s R\varepsilon_{th}/\left[(1-2\nu_s)h_f\right]$. This implies a quite high level of thermal strain at the bifurcation, which would require a large strain framework to be considered for the core. Of course an extremely soft core is unable to induce sufficiently large compressive stresses in the shell. On the contrary, the critical load is much lower in the case of a relatively stiff core ($\varepsilon_{th} \approx 1.1\%$ in Fig. 7).

The circumferential profiles remain constant in the two cases up to large deflections. The established 3D model based on the ANM offers a very high computing speed to reach the critical point with only a few steps, with an adaptive reduction of step length. An accumulation of small steps close to the first bifurcation is observed, but there is nothing similar beyond, which indicates that there is no secondary bifurcation in these two cases.

According to the analytical post-buckling analysis, the subcritical/supercritical transition occurs once for $C_t^* = 15.27$ in the case of boundary conditions $w = 0, N_x = 0$ (**C**3 − **C**4 − **S**3 − **S**4 according to the nomenclature recalled in Eq. (12)). The bifurcation is subcritical below this value, and supercritical beyond this value. Two bifurcation curves are reported in Fig. 13 corresponding to $C_t^* = 13.5$ and $C_t^* = 17.3$, respectively, with the boundary condition **C**3. The results are in accordance with the analytical solution: the first bifurcation is subcritical for $C_t^* = 13.5$ and supercritical for $C_t^* = 17.3$. In the first case, one observes a hysteresis loop and a re-stabilization of the post-buckling path, which were generally re-

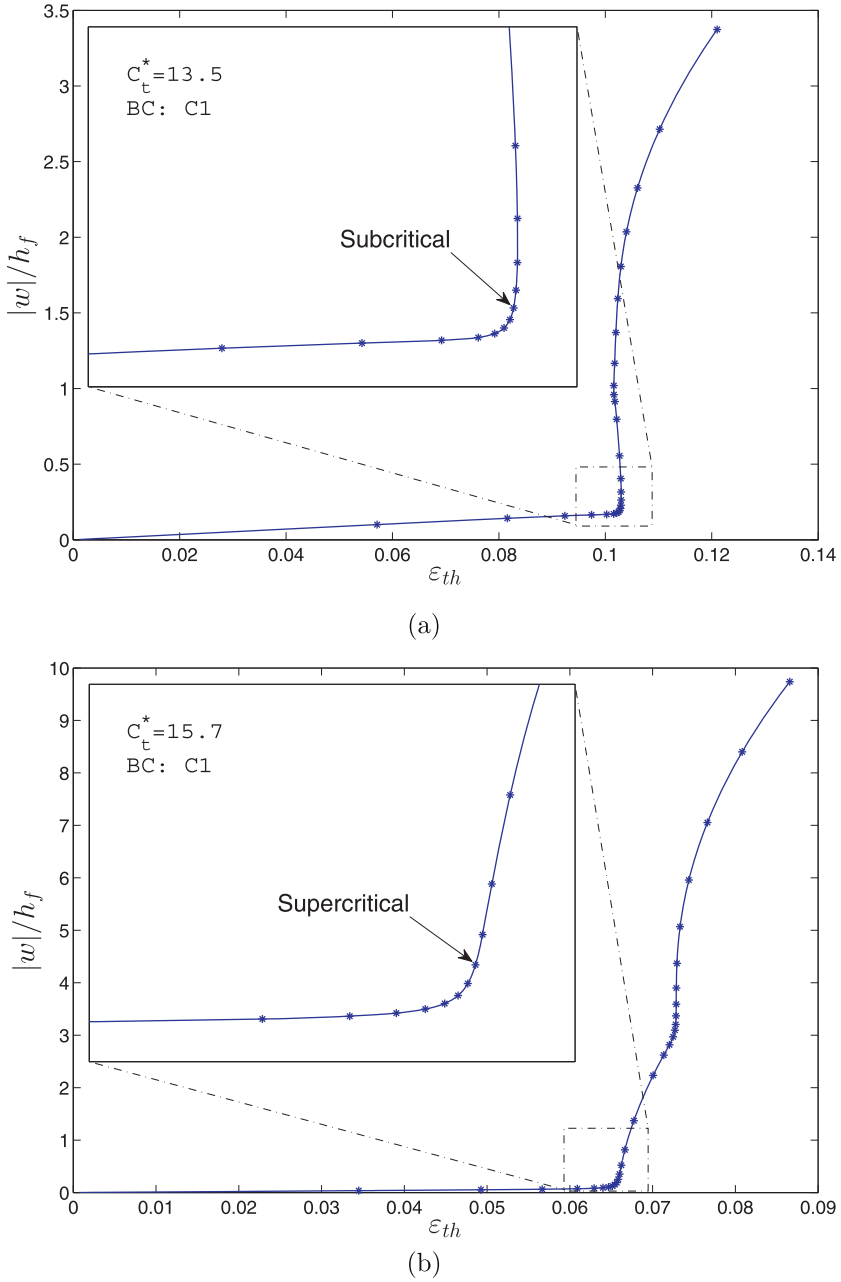

Fig. 15. Comparison of bifurcation diagram between (a) Core-shell V with $C_t^* = 13.5$ and (b) Core-shell VI with $C_t^* = 15.7$. The boundary condition **C**1 is set. ANM parameters: $n = 15$, $\delta = 10^{-6}$. Each point corresponds to one ANM step.

vealed for pure shells under circumferential loadings, *i.e.* lateral or hydrostatic pressure. In the second case with $C_t^* = 17.3$, there is also a hysteresis loop, and an accumulation of small steps near the maximal load ($|w|/h_f = 2.8$ and $\varepsilon_{th} = 0.057$) indicates that this maximum corresponds to a perturbed bifurcation. To understand this quasi-bifurcation phenomenon, we have plotted the deflection at two points A and B chosen in the middle circle ($\theta = 0$ for A and $\theta = \pi/4$ for B as depicted in Fig. 3). Indeed one finds a smooth evolution for the deflection at point A, while there exist strong slope discontinuities for the deflection at point B, as seen in Fig. 14. Hence it turns out that this hysteresis loop is associated with an evolution of the profile along the circumference.

Finite element computations have been performed for the other class of BCs as well, *i.e.* boundary condition **C**1 and $C_t^* = 13.5$ and $C_t^* = 15.7$, as shown in Fig. 15. The results are quite similar to the case of boundary condition **C**3: subcritical/supercritical transition for $C_t^* = 15 \pm 1$, hysteresis loops and re-stabilization of the post-buckling curve, and presence of a quasi-bifurcation for the stiffer core with $C_t^* = 15.7$.

Lastly, we evaluate the influence of the Batdorf parameter by comparing Core-shells I and VII, which hold the same stiffness ratio $C_t^* = 1438$ but different Batdorf parameters $Z = 2133$ and $Z = 528 \approx 2133/4$, respectively. According to Abdelmoula and Leger (2008), the size of the boundary layer is proportional to $1/\sqrt{Z}$. This theoretical result is corroborated by the axial profiles obtained from the finite element model, as shown in Fig. 16. It demonstrates that the boundary layer becomes effectively about twice larger when the Batdorf parameter is divided by 4. Details on the associated wrinkling modes for various cases listed in Table 3 are reported in Supplementary material.

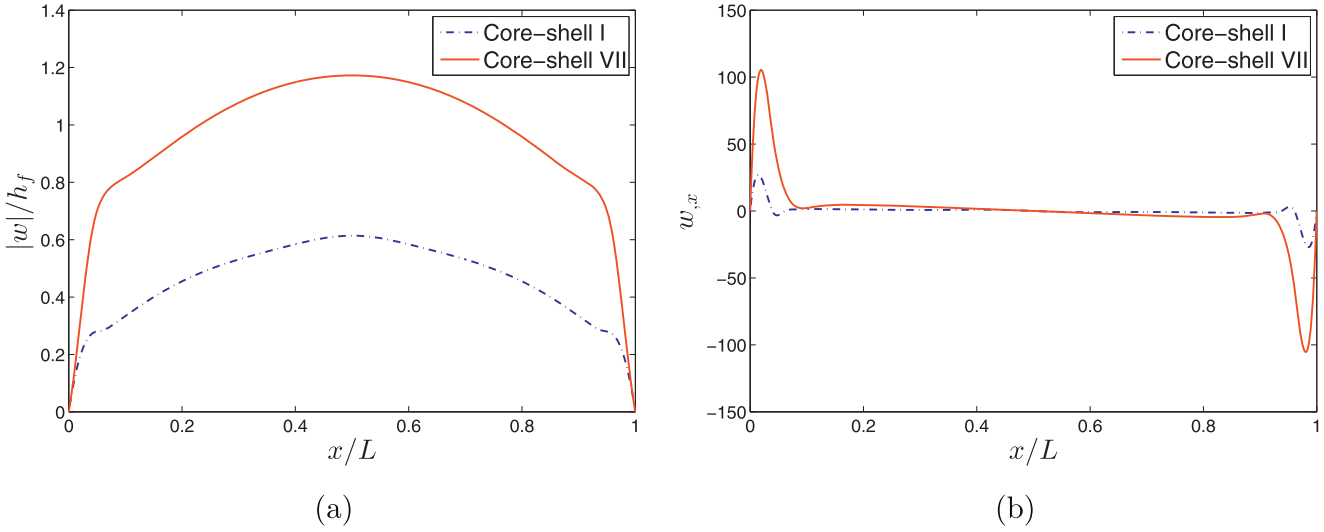

Fig. 16. Comparison of boundary layers at the critical load between Core-shell I with $Z = 2113$ and Core-shell VII with $Z = 528$. The boundary condition **C**1 is imposed.

5. Conclusion

The buckling and post-buckling of cylindrical core-shells subjected to uniform thermal loading were investigated, which completes the previous work on the same curved structure under axial compression (Xu and Potier-Ferry, 2016b). This study has been carried out first from theoretical considerations within the DMV shell theory, then from finite element analyses based on a core described by a linear elastic solid and a surface layer by a nonlinear shell model. In all the studied cases, the instability mode is churro-like, with one half wave in the axial direction and several waves in the circumferential direction, but with a shorter wavelength than that in the axial compression case. In fact, these buckling modes of cylindrical core-shells do not differ significantly from the modes of a pure shell structure without a core, and the deformed shape appears more dependent on geometry and loading than on the presence of the substrate. Indeed the curvature increases the stiffness of cylindrical structures in such a way that their stability is more sensitive to the circumferential compressive stress than the axial one. Roughly the same response could be observed for axially compressed core-shell cylinders (Zhao et al., 2014; Xu and Potier-Ferry, 2016b) or spherical core-shell structures under pressure (Stoop et al., 2015).

The dimensional analysis establishes that the governing equations depend mainly on a dimensionless parameter $C_t = (E_s/E_f)(L/h_f)^{3/2}(R/h_f)^{3/4}$ (or C_t^* defined in Eq. (28)) that measures the relative core stiffness. For a soft core, the first bifurcation is subcritical and turns out to be supercritical for a stiffer core, the turning point being $C_t^* \approx 15$. This result was obtained from an analytical post-bifurcation analysis and confirmed by finite element computations. This stabilization of the post-buckling response is the main contribution of the substrate and it was also observed under other loadings and geometries.

As established in historical studies on pure cylindrical shells, the response of core-shells depends on the famous Batdorf parameter $Z = L^2\sqrt{1-\nu_f^2}/(Rh_f)$ as well, while the Batdorf parameter acts mainly in boundary layers, which leads to boundary effects on the first bifurcation load. Nevertheless, the influence of these boundary layers diminishes in the post-buckling stage. It also decreases when the core stiffness increases, and becomes insignificant for C_t^* larger than 100.

Acknowledgments

This work is supported by the National Natural Science Foundation of China (Grant No. 11602058), Shanghai Education Development Foundation and Shanghai Municipal Education Commission (Shanghai Chenguang Program, Grant No. 16CG01), and the start-up fund from Fudan University. The authors are also grateful for the financial support from the French National Research Agency ANR (LabEx DAMAS, Grant No. ANR-11-LABX-0008-01).

Appendix A. Nonlinear post-buckling calculation

The main objective is to discuss whether the bifurcated branch is supercritical or subcritical. In this respect one calculates analytically the coefficient Σ_2 according to the formulae (39) and (40). By comparing (30) with (37), the two linear operators $\mathcal{L}(.)$ and $\mathcal{L}'(.)$, and the quadratic operator $Q(.,.)$ read

$$\begin{cases} \mathcal{L}\begin{bmatrix} w \\ f \end{bmatrix} = \begin{bmatrix} \dfrac{\partial^4 w}{\partial y^4} - \dfrac{\partial^2 f}{\partial x^2} - \Sigma_0 \dfrac{\partial^2 w}{\partial y^2} + qC_t^* w \\ -\dfrac{1}{12(1-\nu_f^2)}\dfrac{\partial^4 f}{\partial y^4} - \dfrac{\partial^2 w}{\partial x^2} \end{bmatrix}, \\ \mathcal{L}'\begin{bmatrix} w \\ f \end{bmatrix} = \begin{bmatrix} -\dfrac{\partial^2 w}{\partial y^2} \\ 0 \end{bmatrix}, \\ \mathcal{Q}\left[\begin{pmatrix} w \\ f \end{pmatrix}, \begin{pmatrix} w \\ f \end{pmatrix}\right] = \begin{bmatrix} [f,w] \\ \dfrac{1}{2}[w,w] \end{bmatrix}. \end{cases} \tag{41}$$

Now let us describe the differential Eq. (39-b) to get the second term of the asymptotic expansion by starting from the first term $\mathbf{U}_1 = \begin{bmatrix} w_1 \\ f_1 \end{bmatrix} = \begin{bmatrix} \hat{w}(x) \\ \hat{f}(x) \end{bmatrix}\cos(qy)$ obtained in Section 3.6.

$$\begin{cases} \dfrac{\partial^4 w_2}{\partial y^4} - \dfrac{\partial^2 f_2}{\partial x^2} - \Sigma_0 \dfrac{\partial^2 w_2}{\partial y^2} + qC_t^* w_2 = [w_1, f_1], \\ \dfrac{1}{12(1-\nu_f^2)}\dfrac{\partial^4 f_2}{\partial y^4} + \dfrac{\partial^2 w_2}{\partial x^2} = -\dfrac{1}{2}[w_1, w_1]. \end{cases} \tag{42}$$

Since $\mathbf{U}_1$ is harmonic along the y direction, the right-hand sides of (42) combine terms that do not depend on y (harmonic 0) and

terms proportional to $\cos(2qy)$ (harmonic 2):

$$\begin{cases}[w_1, f_1] = -\dfrac{q^2}{2}\left(\hat{w}\hat{f}\right)'' - \dfrac{q^2}{2}\cos(2qy)\left(\hat{w}\hat{f}'' + \hat{w}''\hat{f} - 2\hat{w}'\hat{f}'\right),\\ [w_1, w_1] = -\dfrac{q^2}{2}\left(\hat{w}^2\right)'' - q^2\cos(2qy)\left(\hat{w}\hat{w}'' - \hat{w}'^2\right).\end{cases} \tag{43}$$

Hence, the solution of (42) is expressed in the form

$$\begin{bmatrix}\hat{w}_2(x,y)\\ \hat{f}_2(x,y)\end{bmatrix} = \begin{bmatrix}\hat{w}^{(0)}(x)\\ \hat{f}^{(0)}(x)\end{bmatrix} + \begin{bmatrix}\hat{w}^{(2)}(x)\\ \hat{f}^{(2)}(x)\end{bmatrix}\cos(2qy), \tag{44}$$

in which $w^{(0)}(x)$ and $f^{(0)}(x)$ are solutions of

$$\begin{cases}-f^{(0)''} + qC_t^* w^{(0)} = -\dfrac{q^2}{2}\left(\hat{w}\hat{f}\right)'',\\ w^{(0)''} = \dfrac{q^2}{4}\left(\hat{w}^2\right)'',\end{cases} \tag{45}$$

and $w^{(2)}(x)$ and $f^{(2)}(x)$ are solutions of

$$\begin{cases}\left(16q^4 + 4\Sigma q^2 + qC_t^*\right)w^{(2)} - f^{(2)''} = -\dfrac{q^2}{2}\left(\hat{w}\hat{f}'' + \hat{w}''\hat{f} - 2\hat{w}'\hat{f}'\right),\\ \dfrac{4q^4}{3(1-\nu_f^2)}f^{(2)} + w^{(2)''} = \dfrac{q^2}{2}\left(\hat{w}^2\hat{w}'' - \hat{w}'^2\right).\end{cases} \tag{46}$$

The solution of (45-b) is obvious ($w^{(0)} = q^2\hat{w}^2/4$ eventually depends on boundary conditions). Eq. (46) can be transformed into a differential equation for the deflection. In fact, the stress function can be extracted from Eq. (46-b):

$$f^{(2)} = -\frac{3(1-\nu_f^2)}{4q^4}w^{(2)''} + \frac{3(1-\nu_f^2)}{8q^2}\left(\hat{w}\hat{w}'' - \hat{w}'^2\right). \tag{47}$$

Through introducing it into Eq. (46-a), one gets

$$\begin{aligned}w^{(2)''''} + \sigma^4 w^{(2)} &= \frac{q^2}{2}\left(\hat{w}\hat{w}'' - \hat{w}'^2\right)''\\ &- \frac{2q^6}{3(1-\nu_f^2)}\left(\hat{w}\hat{f}'' + \hat{w}''\hat{f} - 2\hat{w}'\hat{f}'\right),\end{aligned} \tag{48}$$

in which σ is given by

$$\sigma^4 = \frac{4q^4}{3(1-\nu_f^2)}\left(16q^4 + 4\Sigma q^2 + qC_t^*\right). \tag{49}$$

To obtain specific solutions, boundary conditions have to be taken into account.

Case: *prescribed applied force $N_x = 0$ and $w = w_{,x} = 0$ for the simplified model (30)*

In this case the mode can be written as (see Eq. (35-a))

$$\begin{cases}\hat{w}(x) = \cos(\pi x),\\ \hat{f}(x) = \dfrac{12(1-\nu_f^2)\pi^2}{q^4}\cos(\pi x).\end{cases} \tag{50}$$

Now let us compute two quantities in the right-hand side of Eq. (48):

$$\begin{cases}\hat{w}\hat{w}'' - \hat{w}'^2 = -\pi^2,\\ \hat{w}\hat{f}'' + \hat{w}''\hat{f} - 2\hat{w}'\hat{f}' = -\dfrac{24(1-\nu_f^2)\pi^4}{q^4}.\end{cases} \tag{51}$$

Thus, Eq. (48) becomes

$$w^{(2)''''} + \sigma^4 w^{(2)} = 16q^2\pi^4. \tag{52}$$

The solution of the system (45) consequently reads (a useless arbitrary constant is dropped)

$$\begin{cases}w^{(0)} = \dfrac{q^2}{4}\cos^2(\pi x),\\ f^{(0)} = \dfrac{C_t^* q^3}{16}x^2 + \cos(2\pi x)\left(\dfrac{3(1-\nu_f^2)\pi^2}{q^2} - \dfrac{q^3 C_t^*}{32\pi^2}\right).\end{cases} \tag{53}$$

To solve the ODE (52), boundary conditions require to be accounted, two of which are $w^{(2)}(\pm 1/2) = 0$. The condition $N_x = 0$ yields $f^{(2)}(\pm 1/2) = 0$ and through considering Eqs. (46) and (51), one gets

$$\begin{cases}w^{(2)''}(\pm 1/2) = -\dfrac{q^2\pi^2}{2},\\ w^{(2)}(\pm 1/2) = 0.\end{cases} \tag{54}$$

Let us pass to the solution of the boundary value problems (52) and (54). The general solution of (52) reads

$$\begin{aligned}w^{(2)}(x) = \frac{16q^2\pi^4}{\sigma^4}\Bigg[1 + C\cosh\left(\frac{\sigma x}{\sqrt{2}}\right)\cos\left(\frac{\sigma x}{\sqrt{2}}\right) \qquad (55)\\ + D\sinh\left(\frac{\sigma x}{\sqrt{2}}\right)\sin\left(\frac{\sigma x}{\sqrt{2}}\right)\Bigg], \qquad (55)\end{aligned}$$

where the parameters C and D are arbitrary at this level. Next the two boundary conditions in (54) yield (with $\xi = \sigma/2\sqrt{2}$)

$$\begin{cases}C\cosh(\xi)\cos(\xi) + D\sinh(\xi)\sin(\xi) = -1,\\ -C\sinh(\xi)\sin(\xi) + D\cosh(\xi)\cos(\xi) = -\dfrac{\sigma^2}{32\pi^2},\end{cases} \tag{56}$$

which gives the expressions of two constants C and D:

$$\begin{cases}C = \left(-\cosh(\xi)\cos(\xi) + \dfrac{\sigma^2}{32\pi^2}\sinh(\xi)\sin(\xi)\right)/\phi,\\ D = \left(-\sinh(\xi)\sin(\xi) - \dfrac{\sigma^2}{32\pi^2}\cosh(\xi)\cos(\xi)\right)/\phi,\end{cases} \tag{57}$$

where

$$\phi = \cos^2(\xi) + \sinh^2(\xi). \tag{58}$$

From Eqs. (47) and (51), one obtains

$$\begin{aligned}f^{(2)}(x) = -\frac{3(1-\nu_f^2)}{4q^4}\Bigg[\frac{16q^2\pi^4}{\sigma}\Bigg(-C\sinh\left(\frac{\sigma x}{\sqrt{2}}\right)\sin\left(\frac{\sigma x}{\sqrt{2}}\right)\\ + D\cosh\left(\frac{\sigma x}{\sqrt{2}}\right)\cos\left(\frac{\sigma x}{\sqrt{2}}\right)\Bigg) + \frac{\pi^2 q^2}{2}\Bigg].\end{aligned} \tag{59}$$

Hence, the solution at order 2 is completely established. One can compute the coefficient Σ_2 in Eq. (40) from the quadratic operator $Q(.,.)$, the scalar product $\langle .,. \rangle$ being the $L^2(\Omega)\times L^2(\Omega)$-one in the domain $\Omega = [-1/2, 1/2]\times[0, 2\pi/q]$:

$$\Sigma_2 = \frac{2\langle Q(\mathbf{U}_1, \mathbf{U}_2), \mathbf{U}_1\rangle}{\langle \mathcal{L}'(\mathbf{U}_1), \mathbf{U}_1\rangle} = \frac{\int\int_\Omega (2[f_1, w_1]w_2 + [w_1, w_1]f_2)\mathrm{d}\Omega}{\int\int_\Omega \left(\dfrac{\partial w_1}{\partial x}\right)^2 \mathrm{d}\Omega}. \tag{60}$$

Appendix B. Connection between thermal strain and membrane stress

In Section 2, the thermal loading has been represented by an applied uniform residual strain ε_{th} in the core. In the analytical study in Section 3, it has been accounted by a plane uniform isotropic stress state ($\sigma_x = \sigma_y$) in the shell. Of course there is no apparent reason why the stress will be uniform in the surface layer, especially in the post-buckling stage. Nevertheless, it has been proved that the assumption of a uniform membrane stress is almost valid up to the first bifurcation, which will lead to an explicit and simple relation between the thermal strain ε_{th} in the core and the membrane stress in the shell.

First, it has been established numerically that the stress field in the core is nearly uniform and isotropic ($\sigma_{ij}^s \approx \sigma^s\delta_{ij}$), and it is plane and isotropic in the shell ($\sigma_{\alpha\beta}^f = \sigma^f\delta_{\alpha\beta}, \sigma_{i3}^f = 0$), where Latin

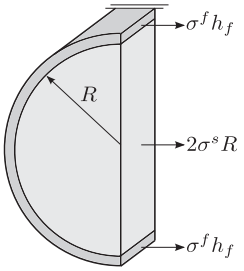

Fig. 17. Equilibrium of forces applied to a half core-shell cylinder.

indices i, j run from 1 to 3, whereas Greek indices α, β take values in $\{1, 2\}$. Second, one can assume that small strain elasticity applies in the pre-buckling stage:

$$\begin{cases} \varepsilon^s_{ij} = \varepsilon_{th}\delta_{ij} + \dfrac{1+\nu_s}{E_s}\sigma^s_{ij} - \dfrac{\nu_s}{E_s}\mathrm{tr}(\sigma^s)\delta_{ij}, \\ \varepsilon^f_{ij} = \dfrac{1+\nu_f}{E_f}\sigma^f_{ij} - \dfrac{\nu_f}{E_f}\mathrm{tr}(\sigma^f)\delta_{ij}, \end{cases} \tag{61}$$

which leads to values of the strains, for instance the strains along Ox:

$$\begin{cases} \varepsilon^s_x = \varepsilon_{th} + \dfrac{1-2\nu_s}{E_s}\sigma^s, \\ \varepsilon^f_x = \dfrac{1-\nu_f}{E_f}\sigma^f. \end{cases} \tag{62}$$

These two strains should be continuous at the interface: $\varepsilon^f_x = \varepsilon^s_x$. Last, the equilibrium of forces applied to a half core-shell cylinder (see Fig. 17) gives a relation between the stress in the shell and the one in the core:

$$\sigma^f h_f + \sigma^s R = 0. \tag{63}$$

Combining these four relations, one can obtain the stress state as a function of the thermal strain:

$$\varepsilon_{th} = \left(\frac{1-\nu_f}{E_f} + \frac{(1-2\nu_s)h_f}{E_s R}\right)\sigma^f = -\left(\frac{(1-\nu_f)R}{E_f h_f} + \frac{1-2\nu_s}{E_s}\right)\sigma^s. \tag{64}$$

References

Abdelmoula, R., Damil, N., Potier-Ferry, M., 1992. Influence of distributed and localized imperfections on the buckling of cylindrical shells under external pressure. Int. J. Solids Struct. 29, 1–25.

Abdelmoula, R., Leger, A., 2008. Singular perturbation analysis of the buckling of circular cylindrical shells. Eur. J. Mech. A–Solids 27, 706–729.

Allen, H.G., 1969. Analysis and design of structural sandwich panels. Pergamon Press, New York.

Allgower, E.L., Georg, K., 1990. Numerical continuation methods. Springer–Verlag, Berlin.

Arbocz, J., 1987. Post-buckling behaviour of structures numerical techniques for more complicated structures. In: Buckling and Post-Buckling: Lecture Notes in Physics 288. Springer–Verlag, Heidelberg, pp. 83–142.

Audoly, B., Boudaoud, A., 2008. Buckling of a stiff film bound to a compliant substrate–part i: Formulation, linear stability of cylindrical patterns, secondary bifurcations. J. Mech. Phys. Solids 56, 2401–2421.

Baguet, S., Cochelin, B., 2003. On the behaviour of the ANM continuation in the presence of bifurcations. Commun. Numer. Methods Eng. 19, 459–471.

Batdorf, S.B., 1947. A simplified method of elastic-stability analysis for thin cylindrical shells. NACA Ann. Rep. 33, 285–309.

Bažant, Z.P., Cedolin, L., 1991. Stability of Structures: Elastic, inelastic, Fracture and Damage Theories. Oxford University Press, New York.

Biot, M.A., 1937. Bending of an infinite beam on an elastic foundation. J. Appl. Mech. 203, A1–A7.

Boutyour, E.H., Zahrouni, H., Potier-Ferry, M., Boudi, M., 2004. Bifurcation points and bifurcated branches by an asymptotic numerical method and padé approximants. Int. J. Numer. Methods Eng. 60, 1987–2012.

Bowden, N., Brittain, S., Evans, A.G., Hutchinson, J.W., Whitesides, G.M., 1998. Spontaneous formation of ordered structures in thin films of metals supported on an elastomeric polymer. Nature 393, 146–149.

Brau, F., Vandeparre, H., Sabbah, A., Poulard, C., Boudaoud, A., Damman, P., 2011. Multiple-length-scale elastic instability mimics parametric resonance of nonlinear oscillators. Nat. Phys. 7, 56–60.

Breid, D., Crosby, A.J., 2013. Curvature-controlled wrinkle morphologies. Soft Matter 9, 3624–3630.

Brush, D.O., Almroth, B.O., 1975. Buckling of bars, plates and shells. McGraw-Hill, New York.

Büchter, N., Ramm, E., Roehl, D., 1994. Three-dimensional extension of non-linear shell formulation based on the enchanced assumed strain concept. Int. J. Numer. Methods Eng. 37, 2551–2568.

Budiansky, B., 1974. Theory of buckling and post-buckling behavior of elastic structures. Adv. Appl. Mech. 14, 1–65.

Bushnell, D., 1985. Computerized buckling analysis of shells. Kluwer Academic Publishers, Dordrecht.

Bushnell, D., Bushnell, B., 2015. Shell buckling. http://shellbuckling.com.

Cai, S., Breid, D., Crosby, A.J., Suo, Z., Hutchinson, J.W., 2011. Periodic patterns and energy states of buckled films on compliant substrates. J. Mech. Phys. Solids 59, 1094–1114.

Cao, Y., Hutchinson, J.W., 2012. Wrinkling phenomena in neo-hookean film/substrate bilayers. J. Appl. Mech. 79. 031019-1–031019-9.

Chan, E.P., Crosby, A.J., 2006. Fabricating microlens arrays by surface wrinkling. Adv. Mater. 18, 3238–3242.

Chen, X., Hutchinson, J.W., 2004. Herringbone buckling patterns of compressed thin films on compliant substrates. J. Appl. Mech. 71, 597–603.

Chen, X., Yin, J., 2010. Buckling patterns of thin films on curved compliant substrates with applications to morphogenesis and three-dimensional micro-fabrication. Soft Matter 6, 5667–5680.

Cochelin, B., 1994. A path-following technique via an asymptotic-numerical method. Comput. Struct. 53, 1181–1192.

Cochelin, B., Damil, N., Potier-Ferry, M., 1994. Asymptotic-numerical methods and pAdé approximants for non-linear elastic structures. Int. J. Numer. Methods Eng. 37, 1187–1213.

Cochelin, B., Damil, N., Potier-Ferry, M., 2007. Méthode asymptotique numérique. Hermès Science Publications, Paris.

Cochelin, B., Medale, M., 2013. Power series analysis as a major breakthrough to improve the efficiency of asymptotic numerical method in the vicinity of bifurcations. J. Comput. Phys. 236, 594–607.

Damil, N., Potier-Ferry, M., 1990. A new method to compute perturbed bifurcation: application to the buckling of imperfect elastic structures. Int. J. Eng. Sci. 26, 943–957.

Doedel, E., 1981. AUTO: A program for the automatic bifurcation analysis of autonomous systems. Congr. Numer. 30, 265–284.

Efimenko, K., Rackaitis, M., Manias, E., Vaziri, A., Mahadevan, L., Genzer, J., 2005. Nested self-similar wrinkling patterns in skins. Nat. Mater. 4, 293–297.

Fu, Y., Cai, Z., 2015. An asymptotic analysis of the period-doubling secondary bifurcation in a film/substrate bilayer. SIAM J. Appl. Math. 75, 2381–2395.

Howarter, J.A., Stafford, C.M., 2010. Instabilities as a measurement tool for soft materials. Soft Matter 6, 5661–5666.

Huang, X., Li, B., Hong, W., Cao, Y.P., Feng, X.Q., 2016. Effects of tension-compression asymmetry on the surface wrinkling of film-substrate systems. J. Mech. Phys. Solids 94, 88–104.

Huang, Z.Y., Hong, W., Suo, Z., 2005. Nonlinear analyses of wrinkles in a film bonded to a compliant substrate. J. Mech. Phys. Solids 53, 2101–2118.

Hutchinson, J.W., Koiter, W.T., 1970. Postbuckling theory. Appl. Mech. Rev. 23, 1353–1366.

Jia, F., Li, B., Cao, Y.P., Xie, W.H., Feng, X.Q., 2015. Wrinkling pattern evolution of cylindrical biological tissues with differential growth. Phys. Rev. E 91. 012403-1–012403-8.

Julien, J.F., 1991. Buckling of shell structures, on land, in the sea and in the air. Taylor & Francis, London.

Karam, G.N., Gibson, L.J., 1995. Elastic buckling of cylindrical shells with elastic cores–i. analysis. Int. J. Solids Struct. 32, 1259–1283.

von Kármán, T., Tsien, H.S., 1941. The buckling of thin cylindrical shells under axial compression. J. Aero. Sci. 8, 303–312.

Koiter, W.T., 1945. On the stability of elastic equilibrium (in dutch with english summary). Thesis Delft, H.J. Paris, Amsterdam. An English translation is available from: http://imechanica.org/node/1400S.

Koiter, W.T., 2009. W.t. Koiter's elastic stability of solids and structures. Cambridge University Press, Cambridge.

Li, B., Jia, F., Cao, Y.P., Feng, X.Q., Gao, H., 2011. Surface wrinkling patterns on a core-shell soft sphere. Phys. Rev. Lett. 106. 234301-1–234301-4.

Li, Y., 2016. Reversible wrinkles of monolayer graphene on a polymer substrate: toward stretchable and flexible electronics. Soft. Matter. 12, 3202–3213.

Mahadevan, L., Rica, S., 2005. Self-organized origami. Science 307, 1740.

Myint-U, T., 1969. Post-buckling behavior of axially compressed core-filled cylinders. Z. Angew. Math. Mech. 49, 423–426.

Patrício, P., Teixeira, P.I.C., Trindade, A.C., Godinho, M.H., 2014. Longitudinal *versus* polar wrinkling of core-shell fibers with anisotropic size mismatches. Phys. Rev. E 89. 012403-1–012403-7.

Rogers, J.A., Someya, T., Huang, Y., 2010. Materials and mechanics for stretchable electronics. Science 327, 1603–1607.
Sáez, P., Zöllner, A.M., 2017. Mechanics reveals the biological trigger in wrinkly fingers. Ann. Biomed. Eng. 45, 1039–1047.
Shao, Z.C., Zhao, Y., Zhang, W., Cao, Y., Feng, X.Q., 2016. Curvature induced hierarchical wrinkling patterns in soft bilayers. Soft. Matter. 12, 7977–7982.
Sobel, L.H., 1964. Effects of boundary conditions on the stability of cylinders subject to lateral and axial pressure. AIAA J. 2, 1437–1440.
Stoop, N., Lagrange, R., Terwagne, D., Reis, P.M., Dunkel, J., 2015. Curvature-induced symmetry breaking determines elastic surface patterns. Nat. Mater. 14, 337–342.
Sun, J.Y., Xia, S., Moon, M.W., Oh, K.H., Kim, K.S., 2012. Folding wrinkles of a thin stiff layer on a soft substrate. Proc. R. Soc. A 468, 932–953.
Teng, J.G., 1996. Buckling of thin shells: recent advances and trends. Appl. Mech. Rev. 49, 263–274.
Teng, J.G., Rotter, J.M., 2006. Buckling of thin metal shells. Taylor & Francis, London.
Terwagne, D., Brojan, M., Reis, P.M., 2014. Smart morphable surfaces for aerodynamic drag control. Adv. Mater. 26, 6608–6611.
Timoshenko, S.P., Gere, J.M., 1961. Theory of elastic stability. McGraw-Hill Book Company, Inc., New York and London.
Vannucci, P., Cochelin, B., Damil, N., Potier-Ferry, M., 1998. An asymptotic-numerical method to compute bifurcating branches. Int. J. Numer. Methods Eng. 41, 1365–1389.
Wang, Q., Zhao, X., 2015. A three-dimensional phase diagram of growth-induced surface instabilities. Sci. Rep. 8, 8887-1–8887-10.
Wolfram, S., 1991. Mathematica: a system for doing mathematics by computer. Addison–Wesley, San Francisco.
Wu, J., Cheng, Q.H., Liu, B., Zhang, Y.W., Lu, W.B., Hwang, K.C., 2012. Study on the axial compression buckling behaviors of concentric multi-walled cylindrical shells filled with soft materials. J. Mech. Phys. Solids 60, 803–826.
Xu, F., Koutsawa, Y., Potier-Ferry, M., Belouettar, S., 2015a. Instabilities in thin films on hyperelastic substrates by 3d finite elements. Int. J. Solids Struct. 69–70, 71–85.
Xu, F., Potier-Ferry, M., 2016a. A multi-scale modeling framework for instabilities of film/substrate systems. J. Mech. Phys. Solids 86, 150–172.
Xu, F., Potier-Ferry, M., 2016b. On axisymmetric/diamond-like mode transitions in axially compressed core-shell cylinders. J. Mech. Phys. Solids 94, 68–87.
Xu, F., Potier-Ferry, M., Belouettar, S., Cong, Y., 2014. 3D finite element modeling for instabilities in thin films on soft substrates. Int. J. Solids Struct. 51, 3619–3632.
Xu, F., Potier-Ferry, M., Belouettar, S., Hu, H., 2015b. Multiple bifurcations in wrinkling analysis of thin films on compliant substrates. Int. J. Nonlinear Mech. 76, 203–222.
Yamaki, N., 1984. Elastic stability of circular cylindrical shells. North–Holland, Amsterdam.
Yao, J.C., 1962. Buckling of axially compressed long cylindrical shell with elastic core. J. Appl. Mech. 29, 329–334.
Ye, L., Lu, G., Ong, L.S., 2011. Buckling of a thin-walled cylindrical shell with foam core under axial compression. Thin Wall. Struct. 49, 106–111.
Yin, J., Chen, X., Sheinman, I., 2009. Anisotropic buckling patterns in spheroidal film/substrate systems and their implications in some natural and biological systems. J. Mech. Phys. Solids 57, 1470–1484.
Zahrouni, H., Cochelin, B., Potier-Ferry, M., 1999. Computing finite rotations of shells by an asymptotic-numerical method. Comput. Methods Appl. Mech. Eng. 175, 71–85.
Zang, J., Zhao, X., Cao, Y., Hutchinson, J.W., 2012. Localized ridge wrinkling of stiff films on compliant substrates. J. Mech. Phys. Solids 60, 1265–1279.
Zhang, C., Li, B., Huang, X., Ni, Y., Feng, X.Q., 2016. Morphomechanics of bacterial biofilms undergoing anisotropic differential growth. Appl. Phys. Lett. 109. 143701-1–143701-5.
Zhao, Y., Cao, Y., Feng, X.Q., Ma, K., 2014. Axial compression-induced wrinkles on a core-shell soft cylinder: theoretical analysis, simulations and experiments. J. Mech. Phys. Solids 73, 212–227.

Supplementary Information

Table S1

Various instability patterns are depicted for core-shell cylinders reported in Table 3 under thermal loading. The analytical wave number n_{cr} well agrees with the numerical wave number n. Note that the wrinkling modes with an odd wave number n_{cr} cannot be exactly recovered by numerical results due to the geometric symmetry consideration in computations.

Core-shell	C_t/C_t^*	Z	n_{cr}/n	Wrinkling patterns
I	266/1438	2113	11/12	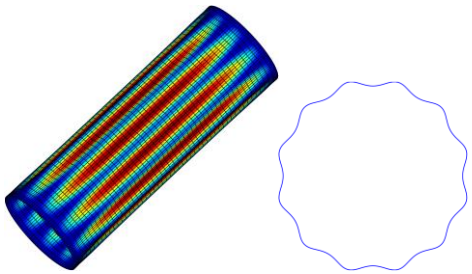
II	0.1/0.5	2113	4/4	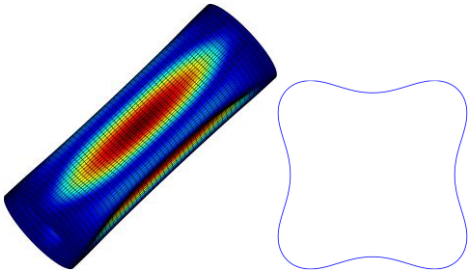
III	2.5/13.5	101	8/8	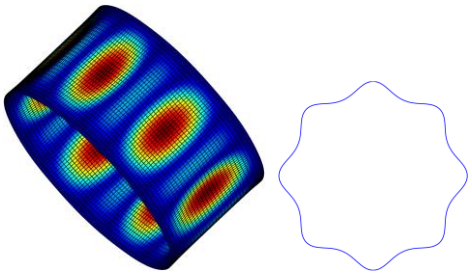
IV	3.2/17.3	1146	3/2	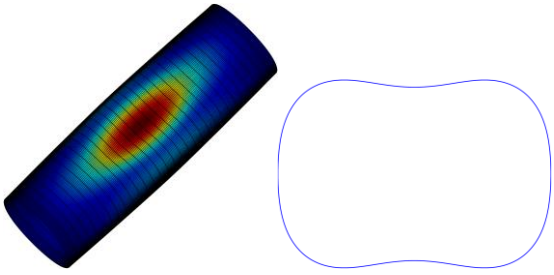

V	2.5/13.5	98	10/10	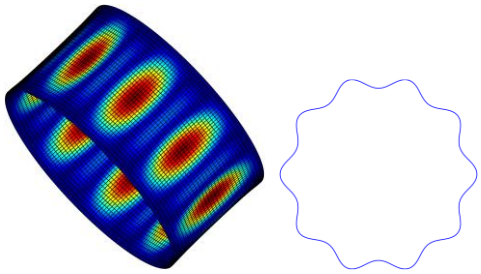
VI	2.9/15.7	1309	3/2	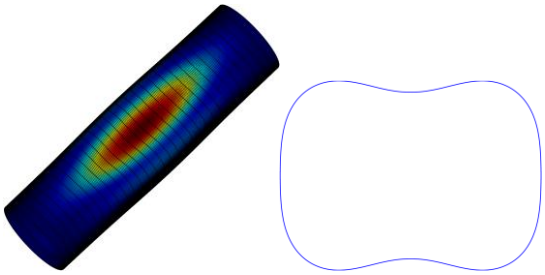
VII	266/1438	528	16/18